Patrick Kraus, BSc

Measurements of the He-Bi(111) interaction potential using elastic helium atom scattering

Master Thesis

for obtaining the academic degree
Master of Science

Masterstudium Technische Physik

Graz University of Technology

Graz University of Technology

Supervisor:
Univ.-Prof. Mag. Dr.rer.nat Wolfang E. Ernst
Institute of Experimental Physics

Graz, 10 2011

Kurzfassung

Das Verhalten von Kristalloberflächen unterscheidet sich signifikant von denen des Bulk. Die Kristallsymmetrie is plötzlich gebrochen und da die Oberflächenatome keine Bindungspartner mehr haben, werden die Kraftverhältnisse und die elektronischen Eigenschaften der Oberfläche völlig verändert. Materialoberflächen sind von größter technischer Bedeutung. Alle chemischen Reaktionen und Interaktionen mit der Außenwelt finden an der Oberfläche statt. Deshalb ist das Verständnis ihrer Eigenschaften von größter Priorität.

Heliumatomstreuung ist ein einzigartiges Werkzeug um Materialoberflächen zu untersuchen. Es ist nicht nur völlig oberflächensensitiv, sondern es erreicht auch die niedrigen Streuenergien die benötigt werden um die Vibrationsmoden von schweren Metallatomen zu untersuchen. Das elastische Streuspektrum enthält viel Information über das Interaktionspotential zwischen dem Heliumatom und der Oberfläche.

In dieser Arbeit werden elastische Heliumstreuspektren der Bi(111) Oberfläche präsentiert. Unter Verwendung dieser wird ein vollständiges Bild des He-Bi(111) Interaktionspotentials erstellt. Die elastischen Streupeaks und deren Höhen werden benutzt um die Korrugation der Oberfläche zu berechnen. Hierfür wird eine iterative Prozedur angewendet, die im Laufe dieser Arbeit entwickelt wurde. Weiters wurden die winzigen Ausprägungen der elastischen Resonanzen identifiziert und benutzt, um den weltweit ersten Ausdruck des vertikalen Interaktionspotentials zwischen Helium und Bismuth zu berechnen.

Während die Korrugationsfunktion, welche in dieser Arbeit bestätigt wird, für ein Material mit leitender Oberfläche extrem ungewöhnlich ist, ist der Potentialtopf des vertikalen Interaktionspotentials von vergleichbarer Tiefe wie bei anderen Metallen.

Abstract

Crystal surfaces show completely different behavior than the bulk. The crystal symmetry is suddenly broken and since for surface atoms there is no bonding partner any more, the force constants and electronic states at the surface can change significantly. The surfaces of materials are of high technical importance. All of the chemical reactions and the interactions with the outside occur at the surface. So the understanding of its properties is of outstanding importance.

Helium atom scattering is a unique tool to investigate material surfaces. It isn't just completely surface sensitive, but it also reaches the low incident energy to investigate the vibrational modes of heavy metal atoms. The elastic scattering spectrum contains a lot of information about the interaction potential between the helium atom and the surface.

In this work elastic helium scattering spectra of the Bi(111) surface are presented. Using only these a complete picture of the He-Bi(111) interaction potential is obtained. The elastic scattering peaks and their height are used to calculate the electronic surface corrugation applying a new iterative procedure that was developed during the course of this work. Furthermore the diminutive features caused by elastic resonances are identified and used to calculate the very first expression for the vertical interaction potential between helium and bismuth.

Whilst the high corrugation confirmed in this work is extremely unusual regarding an electrically conducting surface, the vertical interaction potential-well is of comparable depth to other metals.

Deutsche Fassung:
Beschluss der Curricula-Kommission für Bachelor-, Master- und Diplomstudien vom 10.11.2008
Genehmigung des Senates am 1.12.2008

EIDESSTATTLICHE ERKLÄRUNG

Ich erkläre an Eides statt, dass ich die vorliegende Arbeit selbstständig verfasst, andere als die angegebenen Quellen/Hilfsmittel nicht benutzt, und die den benutzten Quellen wörtlich und inhaltlich entnommene Stellen als solche kenntlich gemacht habe.

Graz, am ……………………………   ………………………………………………..
(Unterschrift)

Englische Fassung:

STATUTORY DECLARATION

I declare that I have authored this thesis independently, that I have not used other than the declared sources / resources, and that I have explicitly marked all material which has been quoted either literally or by content from the used sources.

……………………………   ………………………………………………..
date   (signature)

Contents

List of Figures

1. Introduction

Helium Atom Scattering (HAS) is a powerful tool to investigate materials surfaces, and has been used during the past decades[1,2]. Using HAS, one can not only determine the structural parameters, but also measure a variety of other surface properties as for example the surface phonon dispersion or the particle-surface interaction potential[3]. HAS has several advantages compared to other methods used for surface investigation such as electron energy loss spectroscopy (EELS) or X-ray photoelectron spectroscopy (XPS) since HAS is purely surface sensitive and nondestructive. The high surface sensitivity results from properties of the probe atoms: The He atom is already repelled by a very low electron density, consequently from the topmost layer. Elastic HAS spectra thus do not map the surface atomic corrugation, but the electron density corrugation on the surface[4,5].

During the past decades HAS has been widely used to investigate the surfaces of ionic crystals, semiconductors and metals. In the first case the strongly located electron densities show a high corrugation whereas in the case of metals HAS measurements just reveal a completely flat electron density. Whereas these materials have been widely investigated using HAS, there exist hardly any measurements on semimetals with the exception of graphite[6–8].

Unfortunately, even with advanced techniques such as a pseudo-random chopper, the measurements of inelastic surface properties take a lot of time. Therefore a very important question is how much information can be extracted out of the elastic measurements. The first step in the analysis of elastic scattering spectra is the determination of the geometric surface structure by analyzing the positions of the scattering peaks. By a careful study of the scattering peak heights it is also possible to determine the electron density surface corrugation. But there is much more information encrypted in tiny bumps of what is widely considered to be a static background. By studying these features even inelastic effects via kinematical focussing[1,3] can be investigated. But of capital importance is the fact that the little peaks and dips contain information about the vertical interaction potential of the sample and the probe atom, giving rise to a complete picture of the interaction potential.

Knowledge of this interaction potential is highly desireable, since the probe atom also undergoes an acceleration before interacting with the repulsive part of the surface, causing a change of the kinetic energy of the helium atom and thus a different scattering angle[1]. Hence, the more detailed understanding of the static background gives rise to a more accurate analysis of the scattering peaks.

Bismuth is a material that is very well suited for an investigation with HAS. It is not only a semimetal, but also the electronic properties of the bismuth surfaces differ fundamentally from those of the bulk[9,10]. Even superconductivity was dicovered in Bi clusters, nanowires and bicrystals[11–13]. Furthermore the large spin-orbit coupling in bismuth makes it very interesting for future applications in spintronics[14] but hinders the ab initio simulations of the materials properties[15].

2. Theoretical Background

2.1. The Description of Materials Structures

Many materials such as metals or salts are built in a simple periodic structure, called a crystal. The major advantage of a simple periodic structure is that the description of the positions of the atoms can be simplified to the coordinates of one or more atoms in one of the smallest units of the periodic structure.
Those smallest units, called the unit cells of the crystal, are arranged in a periodic way. This lattice is defined by three fundamental translation vectors $\mathbf{a}_1, \mathbf{a}_2, \mathbf{a}_3$. Those vectors are chosen in a way that the crystal is mapped into itself by performing a translational shift of

$$\mathbf{r}' = \mathbf{r} + u_1\mathbf{a}_1 + u_2\mathbf{a}_2 + u_3\mathbf{a}_3 \tag{2.1}$$

with u_1, u_2, u_3 being integers. This translational invariance in three dimensions defines a lattice. In three dimensions, there are only 14 different lattice types possible[16]. Since the crystal is perfectly periodic with respect to lattice translation vectors, one only has to describe the atomic positions within the parallelepiped described by the fundamental translation vectors $\mathbf{a}_i$, set upon one lattice point. The resulting cell of the crystal is called the primitive cell. It is a minimum-volume cell that fills all space by periodic repetition. Within the primitive or 'unit' cells, the number and the positions of all atoms are the same. The position of the atoms with respect to the origin of the cell is given by the so-called basis vectors that can be written as linear combination of the fundamental translation vectors

$$\mathbf{r} = b_1\mathbf{a}_1 + b_2\mathbf{a}_2 + b_3\mathbf{a}_3 \tag{2.2}$$

with $0 < b_i < 1$.

With the knowledge of the positions of the unit cells, given by the lattice translation vectors, and the positions of the atoms within the unit cells, given by the basis vectors, one can describe the coordinates of every atom in an infinite crystal.

2.2. The Description of Materials Surfaces

At the surface of a crystal, things change dramatically. Not only the crystal symmetry is suddenly broken, but also the chemical equilibrium that was achieved in the bulk is no longer possible. Thus the investigation of material surfaces is a promising field of research. In order to be able to study material surfaces, one has to be able to distinguish and label the different possible planes. The Miller-Index system is the dominant kind of labeling the surfaces of a crystal. In this system, the orientation of the plane is specified as follows:[17]

- Visualize the plane in a coordinate system spanned by the translational lattice vectors. Find the interception distances of the origin to the plane along the directions $\mathbf{a}_i$ in terms of $\mathbf{a}_i$
- Take the reciprocal values of those numbers and reduce those numbers to the smallest integers with the same ratio.
- If the plane intersects one lattice vector at infinity, the reciprocal is set to zero.
- The resulting numbers (hkl) are called the Miller indices.

The choice of brackets is extremely important in this case. Parentheses () indicate an arbitrary plane just described by the Miller indices, if curly brackets { } are used one usually wants to label the resulting plane as a plane with a very high symmetry as for example the 100 plane in a cubic crystal. Square brackets label directions and not planes. The [102] direction for example labels the $\mathbf{a}_1 + 2\mathbf{a}_3$ direction.

As pointed out above, the conditions for the positions of the atoms at the surface are not quite as easy as in the bulk, in addition to a very severe break of symmetry, also the chemical bonds at the surface are broken, giving rise to dangling bonds and a lot of potential problems or unexpected changes. The two primary alterations of the surface structure to the bulk structure are called reconstruction and relaxation.
Relaxation is an effect mainly due to the additional freedom gained for an atom at the surface and means the change of the interlayer spacing in between the first and the second layer of the material in comparison to the bulk values. Reconstruction, on the other hand, is more complicated. A surface can be reconstructed or unreconstructed. If the surface is unreconstruted, the positions of the atoms at the surface are the same as in the bulk. However, especially the broken covalent or ionic bonds at the surface cause a reconstruction of the surface. In this process, the different atoms bind to each other and thus change the interatomic force constants within the first layer. A possible

consequence are different atomic positions and also very often the appearence of superstructures. In many experiments hydrogen is adsorbed at the surface in order to surpress the effects of dangling covalent bonds.[18,19]

Atomic positions at surfaces, being two-dimensional, can again be described by the superposition of a lattice grid and the basis vectors. Since the surface planes don't have to be parallel to the planes defined by a pair of translational bulk lattice vectors, the surface lattice can have a different structure than the bulk lattice. Again, the two dimensional periodic structure is described by a lattice:

$$\mathbf{r}' \;=\; \mathbf{r} \;+\; c_1\mathbf{A}_1 \;+\; c_2\mathbf{A}_2 \tag{2.3}$$

As in many other aspects of surface description, the nomenclature of Cabrera et al. is adapted here. Using this nomenclature, surface specific vectors are written in capital letters whereas small letters are used for the bulk vectors.

2.3. Scattering Experiments and the Reciprocal Lattice

Since the crystal structure and the structure of the surface affect the properties of the material, it is highly preferable to know the structure before thinking about using the material for any application. Especially the surface structure is very important to most applications, since all of the chemical reactions take place at the surface. For this reason, methods to measure those properties are very important and also very common around materials scientists. Since both the crystal and its surface are periodic structures in three and two dimensions respectively, the interference pattern of a scattered wave provides all the necessary information to determine the structure. Waves are reflected from a periodic structure according to Bragg's law:

$$2d\sin\theta \;=\; n\lambda \tag{2.4}$$

The condition for the existence of reflection is that the incoming wave should have a wavelength smaller than $2d$ with d being the periodicity constant of the crystal. For typical crystal lattice constants d is in the range of a few Å, so we can not scatter visible light from it. The photon energies needed in scattering experiments are usually in the X-ray range and can cause secondary effects when depositing this large amount of energy in the crystal. Using De Broglies equation, one can relate the momentum of a particle with a certain wavelength

$$\lambda \;=\; \sqrt{2mE} \tag{2.5}$$

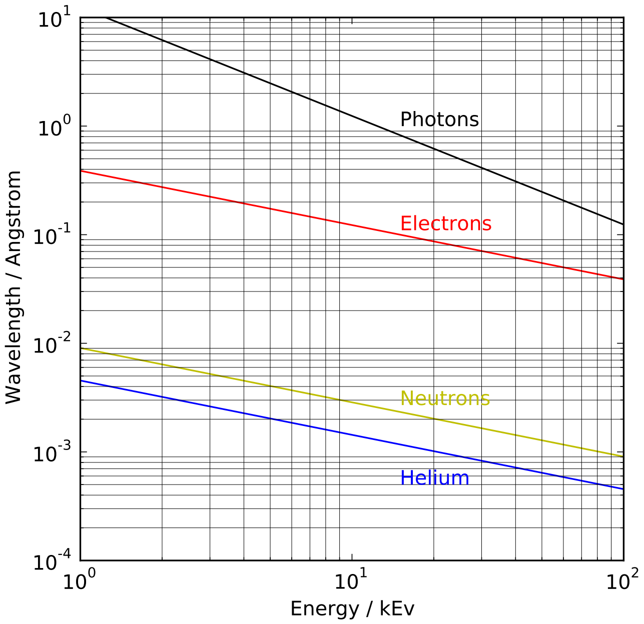

Figure 2.1.: Wavelength dependence of the energy for photons, electrons, neutrons and helium atoms

Since the mass is indirectly proportional to the wavelength, one needs less energy using heavier particles in order to reach the same wavelength. This is shown in figure 2.1. However, scattering particles can be more complicated since there is no way to guarantee a monochromatic and equidirectional beam of particles, especially in the case of electrons, where the particles carry a charge this can be rather bothersome.

Since the particles are scattered from a defined lattice structure, the position of the scattering peaks should be related to this structure and one should be able to calculate the parameters using an elastic scattering spectrum. This can actually be done using a straightforward approach with the Fourier analysis. This kind of analysis is perfectly suited to deal with the periodic conditions we approach in a crystal. Performing such an analysis using not only Fourier transform but also the symmetries of the crystal is easily done and can be read in Kittel[16]. The well known solution is that a scattering peak appears when the momentum of the incoming wave/particle and the momentum of the outcoming one only differ by a reciprocal lattice vector $\mathbf{g}$:

$$\Delta\mathbf{k} = \mathbf{g} \tag{2.6}$$

$$\mathbf{g} = v_1\mathbf{b}_1 + v_2\mathbf{b}_2 + v_3\mathbf{b}_3$$

Where $\mathbf{b}_1$, $\mathbf{b}_2$ and $\mathbf{b}_3$ are the reciprocal lattice vectors

$$\mathbf{b}_1 = 2\pi\frac{\mathbf{a}_2 \times \mathbf{a}_3}{\mathbf{a}_1 \cdot \mathbf{a}_2 \times \mathbf{a}_3}, \quad \mathbf{b}_2 = 2\pi\frac{\mathbf{a}_3 \times \mathbf{a}_1}{\mathbf{a}_1 \cdot \mathbf{a}_2 \times \mathbf{a}_3}, \quad \mathbf{b}_3 = 2\pi\frac{\mathbf{a}_1 \times \mathbf{a}_2}{\mathbf{a}_1 \cdot \mathbf{a}_2 \times \mathbf{a}_3} \tag{2.7}$$

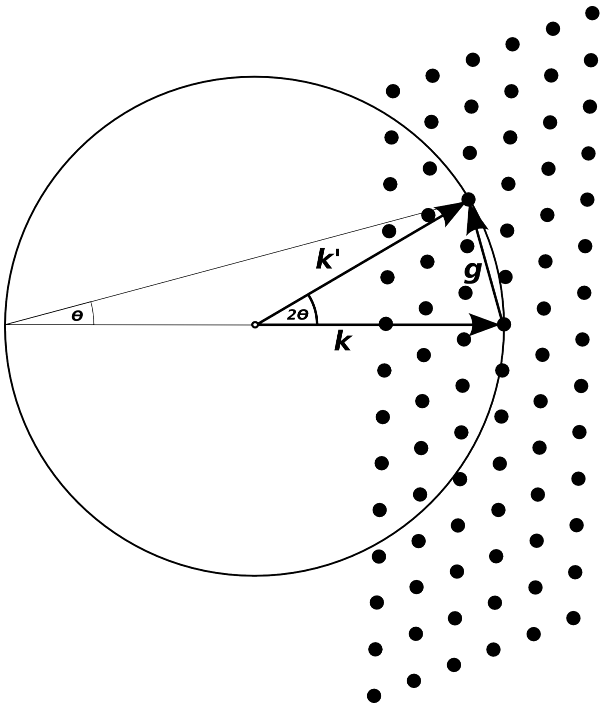

Figure 2.2.: Visualisation of the Bragg condition using the Ewald construction

and the v_i are integers.
One is usually interested in elastic scattering processes which means that the magnitude of the in- and the outgoing momentum stays constant, thus there should be no energy transition involved. Hence,

$$(\mathbf{k} + \mathbf{g})^2 = \mathbf{k}' \text{ or} \tag{2.8}$$

$$2\mathbf{k} \cdot \mathbf{g} = g^2$$

This relation can be shown to be another representation of the Bragg condition 2.5. Also, this representation allows a simple visualisation of the condition in k-space: A scattering peak occurs, when the circle defined by the incoming momentum hits two reciprocal lattice points at once. This is shown as a projection onto two dimensions in figure 2.2. The iso-energy sphere (or circle in the figure) is called the Ewald-sphere. Using these facts, one can calculate the corresponding **g**-vector for an experimentally determined scattering angle and obtain the reciprocal lattice vectors. Knowing those, one can not only calculate the crystal structure in real space, but also determine the atomic spacing of this lattice.

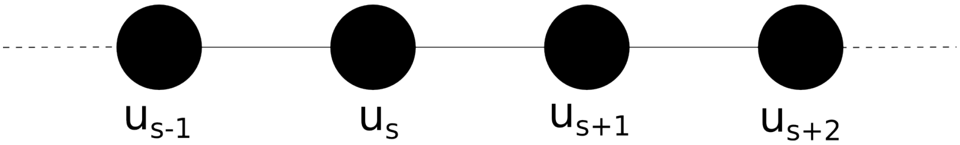

Figure 2.3.: One dimensional chain of atoms connected by Hookean springs

2.4. Lattice Vibrations

To understand the properties of vibrations in crystals, one first has to think about the forces in between the atoms. Since an unperturbed crystal can be assumed to have all atoms in equilibrium positions, there should not be any force acting on the single atoms. If one moves a single atom, the force acting on it can be approximated as being linear, as long as the deformation is small. Since the forces can be assumed as linear, one can think of the crystal as a lattice of atoms of masses M with an equilibrium lattice spacing of a connected by Hookean springs with the force constants C.

The force F_s acting on the displaced atom s (displacement u_s) is:

$$F_s \;=\; C(u_{s+1} - u_s) \;+\; C(u_s - u_{s-1}) \tag{2.9}$$

Thus the equation of motion reads:

$$M\frac{d^2u_s}{dt^2} \;=\; C(u_{s+1} \;+\; u_{s-1} \;-\; 2u_s) \tag{2.10}$$

The only relevant solutions are equivalent to plane waves, so the time dependence is $exp(i\omega t)$. Putting this in the equation of motion, it now reads:

$$-M\omega^2 \;=\; C(u_{s+1} \;+\; u_{s-1} \;-\; 2u_s) \tag{2.11}$$

This is a difference equation and its solutions are travelling waves of the form:

$$u_{s\pm1} \;=\; u \cdot \; exp(isKa)\; exp(\pm Ka) \tag{2.12}$$

with K being the wavevector and a being the spacing in between the atoms. With this solution one easily obtains the dispersion relation for the angular frequency ω:

$$\begin{aligned} \omega^2 \;&=\; \frac{2C}{M}(1 \;-\; cos(Ka)) \text{ or} \\ \omega \;&=\; \sqrt{\frac{4C}{M}}\left|sin\left(\frac{Ka}{2}\right)\right| \end{aligned} \tag{2.13}$$

The main features of this solution are that it starts linear from zero and thus vanishes at the origin (the so-called Γ-point) and reaches its maximum at $K \;=\; \frac{\pi}{a}$, the Brillouin zone boundary. After the boundary the function is just a mirrored version of itself and

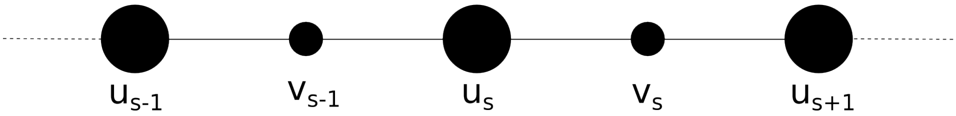

Figure 2.4.: One dimensional diatomic chain of atoms connected by Hookean springs

then just repeats periodically.
This approximation surely is pretty far from reality, since it assumes not only linear forces, but also a one dimensional chain of identical atoms as shown in figure 2.3. Anyhow, the major properties as for example the periodicity apply to all crystals and all directions. To generalize the model a bit, one considers a one dimensional crystal structure with two different atoms per unit cell.

Having two different atoms in each unit cell, as shown in figure 2.4, results in a system of two coupled differential equations by the very same procedure as the case of one atom gave rise to the differential equation before. The system now reads:

$$M_1 \frac{d^2 u_s}{dt^2} = C(v_{s+1} + v_{s-1} - 2u_s) \tag{2.14}$$

$$M_2 \frac{d^2 v_s}{dt^2} = C(u_{s+1} + u_{s-1} - 2v_s) \tag{2.15}$$

Applying the same restrictions to the solution as before, one eventually reaches the condition for allowed vibrational modes:

$$M_1 M_2 \omega^4 - 2C(M_1 + M_2)\omega^2 + 2C^2(1 - cos(Ka)) = 0 \tag{2.16}$$

Figure 2.5 displays the dispersion relation obtained from this condition. The main difference now is that besides the phonon branch that vanishes at the Γ-Point, there is also a second one that doesn't vanish. The vanishing branch is called the acoustic, the other one the optical phonon branch.
This approximation is still just valid for the one dimensional chain of atoms, a situation that is barely achievable. However, in a majority of cases there are high symmetry directions in a crystal where the movement of a crystal plane reduces to a one dimensional problem. In this case the approximation holds. In all the other directions, more complex forces have to be calculated, involving a higher number of contributing crystal atoms.
Additionally, the number of possible phonon branches depends on the dimension of the problem. In a three dimensional crystal, each atom has three degrees of freedom, one for each displacement in the x, y and z directions. If there are p atoms in the primitive cell, the phonon dispersion shows 3 acoustical branches and $3p - 3$ optical ones. Due to symmetry operations in the crystal, the branches can be degenerate, figure 2.6 shows this case for germanium in the [111] direction.

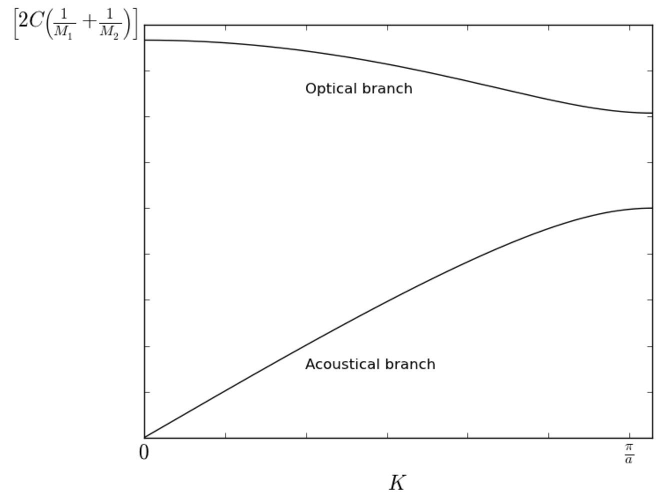

Figure 2.5.: Dispersion relation of the one dimensional diatomic chain of atoms obtained by solving equation 2.16. In a diatomic chain not only the acoustical branch but also the optical branch appear

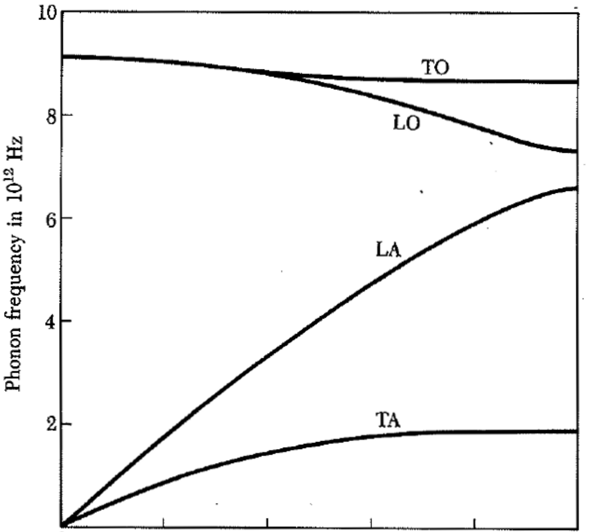

Figure 2.6.: Bulk phonon dispersion relation of germanium in the [111] direction. Depending on the displacement directions the phonon modes are labeled transversal (T) or longitudinal (L) for each of the acousitc (A) and optical (O) modes. From Kittel 1996[16]

The different branches can be labeled by the direction of oscillation. For every possible mode in three dimension there are two transversal branches (labeled TA for Transversal acoustic and TO for transversal optical) and one longitudinal branch (labeled LA and LO). In the case of germanium, shown in figure 2.6 the transversal modes are degenerate due to the crystal symmetry.

Elastic waves in a crystal are described by a Hamiltonian equivalent to the one of a harmonic oscillator (for more detailed information read appendix C of Kittel[16]). Thus, the energy of a lattice vibration is quantized and can only be added or reduced in finite values. The energy quantum of a lattice vibration is called a phonon. The energy of a vibrational mode with angular frequency ω can be written as

$$\epsilon = \left(n + \frac{1}{2}\right)\hbar\omega \tag{2.17}$$

with n being the total number of phonons in this state. A lot of important properties of materials depend on the number and the energy of occupied phonon states, such as the heat capacity or the thermal conductivity, since the movement of the crystal atoms due to thermal energies can be described as thermally excited phonons. For further information on this topic the author recommends chapter 5 of Kittel[16].

2.5. Surface Phonons

The conditions for phonons dramatically change if a surface is introduced. The presence of a surface of the crystal destroys the symmetry in one direction and requires a much more complicated analysis, that is neglected in this work. The basics of surface vibrational research and the analysis of localized surface modes were first published by Lord Rayleigh. His work is generally accepted as the starting point of surface vibrational research. The surface, being basically a two dimensional object, at first seems very easy to describe. The calculations of the phonons on an infinite two dimensional lattice of atoms is also easier than the equivalent calculation in the bulk, but it gives rise to completely wrong solutions. The very important point a newcomer to the field misses at first, is that the surface, though being a two dimensional object, is produced by cutting a three dimensional object in half. So it is insuffcent to study the surface alone, ignoring the underlying layers. In fact, one has to study a semi-infinite crystal in order to understand all the properties of the surface.

As mentioned before, in this work the nomenclature of Cabrera et al is used where capital letters denote surface specific values and z is defined as the direction perpendicular to the surface.

The break of symmetry severely changes the view of phonon branches at the surface.

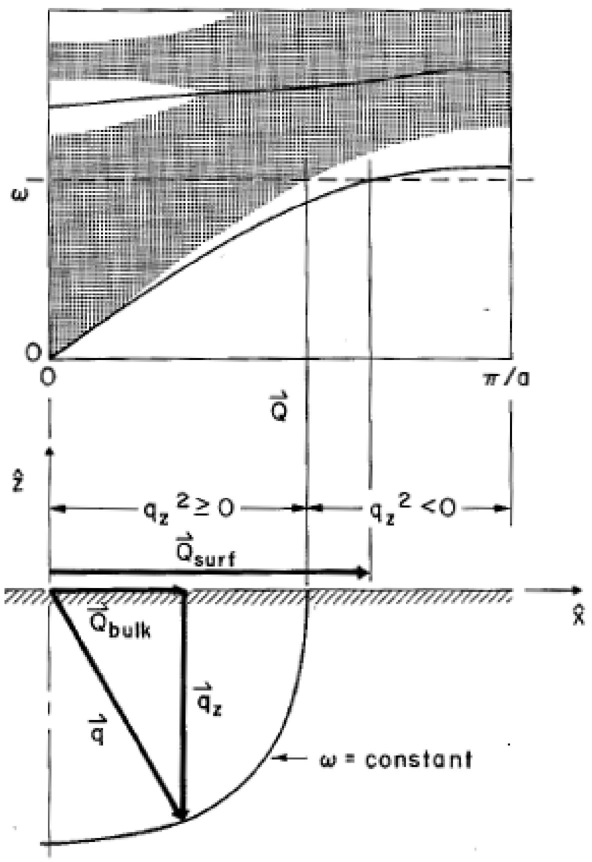

Figure 2.7.: Schematic representation of the origin of bulk bands. By projection of bulk phonon momenta **q** to the surface, its surface component $\mathbf{Q}_{bulk}$ contributes to the surface phonon dispersion. From Scoles, chapter by Doak 1992[20]

The different phonons from the bulk branches can also reach the surface and get reflected at it, contributing to the surface phonon dispersion. All of those bulk phonons have to be described in surface coordinates to calculate the dispersion relation.

Since a surface phonon momentum **Q** can be reached by different bulk momenta **q** projected to the surface, the phonon branches in the bulk add up to a phonon band at the surface, as shown in figure 2.7. If only a finite number of underlying layers is considered, as usual in slab calculation methods to simulate the surface phonon dispersion, one can calculate the single phonon branches that are projected to the surface instead of the band. This is shown in figure 2.8 for lithium flouride (LiF). As the number of layers rises, those branches get increasingly closer to each other and finally form the bulk bands. Besides the bulk bands one can observe localized phonon branches as in the bulk case. Those branches correspond to phonon states with a purely imaginary perpendicular momentum component q_z. The phonons corresponding to those branches show an exponentially decreasing amplitude within the crystal and are thus localized at

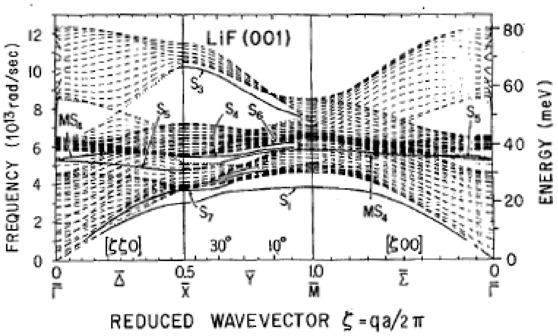

Figure 2.8.: Slab calculations of surface phonon dispersion relations for LiF(001). The bands originate from projected bulk bands. The surface specific phonon modes are labeled S_x From Scoles, chapter by Doak 1992[20]

the surface. Those purely surface specific modes are called Rayleigh modes, since Lord Rayleigh first calculated them for an elastic isotropic medium.

2.6. Helium Atom Scattering from Surfaces

The first particle scattering experiments were performed in order to prove the de Broglie relation, which predicts an energy-dependent wavelength for a particle. These first experiments were carried out using H_2 and He scattering from lithium flouride or NaCl[21]. Since vacuum and surface preparation technologies were not that advanced at that time, the experiments were rather complicated and expensive and received very little attention. As in the 1960's those techniques advanced, and scientists hoped for further enhancement of surface technologies, the particle surface experiments received a lot of attention. Atomic or molecular scattering from surfaces has many advantages compared to other surface-investigation methods, which are:

- Atomic scattering is strictly surface sensitive. Other technologies such as EELS (Electron Energy Loss Spectroscopy) have a more or less large penetration depth of 2-3 surface layers, whereas in atomic scattering only the top layer contributes to the scattering events.

- Due to the very low energies of thermal atoms in the region of 5-300 meV, the scattering is purely non-destructive.

- The usage of noble gases like He, Ne or Ar not only eases the detection of the scattered atoms (due to their low natural background), but also takes advantage of their chemical inertness.

- Probe atoms like He are furthermore spherical, thus carrying no angular or magnetic momentum. They have also very little mass, so that multiple phonon processes are suppressed.

On the other hand, the scattering of atomic beams also yields some disadvantages, that should not be left out. The most significant disadvantage is that atoms are comparatively big and slow. While other probe materials like electrons, light or even neutrons produce an impulsive, local deformation, atoms produce a more extensive deformation. Those deformations can be described as a sum of normal modes. In the classical description this is done with a sum of Fourier coefficients, each one bound to a special frequency. While for the more localized deformation one needs a lot of high frequency coefficients, extended deformations only need coefficients of lower frequencies. This results in an effective frequency cut-off. Using atoms it is increasingly difficult to interact with higher frequencies.[22]

Unlike other experimental methods, atomic scattering from surfaces does not yield the position of the atom cores. Due to the low energies, the atoms are repelled from the electron density a few Angstrom above the first surface layer due to the Pauli repulsion[23–25]. In ionic crystals like the first investigated LiF or NaCl, the electronic density is strongly localized at the core positions, hence in this case there is hardly any difference. In metals on the other hand, the surface electronic density is smooth, resulting in the absence of elastic scattering peaks. Therefore, on low-index metal surfaces elastic scattering peaks only appear in rare cases[26], so there the measurement of surface phonons using inelastic scattering is dominant.

Elastic scattering as described in 2.3 only occurs at certain angles, that are related to the surface structure. But in between those scattering peaks there also exists a signal. The helium atoms can reach those angles by scattering inelastically from the surface via interaction with a surface phonon. The former scattering conditions in equation 2.8 are altered to:

$$\mathbf{K_f} = \mathbf{K_i} + \mathbf{G} + \mathbf{Q} \text{ and} \tag{2.18}$$

$$\mathbf{k_f}^2 = \mathbf{k_i}^2 \pm \hbar\omega(\mathbf{Q}) \tag{2.19}$$

with $\omega(\mathbf{q})$ being the energy of the surface phonon according to its dispersion and the capital letters indicating the surface specific variables. The main problem in measuring the surface phonon dispersion out of the signal in between the elastic scattering peaks is that the energy of the phonon does not affect the angular distribution of the scattered helium atoms, but their velocities. So the method to measure phonon dispersion relations using helium atom scattering is to choose a certain angular position which determines the phononic $\mathbf{Q}$-Vector that can be measured. The speed of the helium atoms changes according to the phonon energy. This speed can be measured using a time of flight measurement. For a more detailed view of the subject the author recommends[22,27,28].

There are basically two different kinds of helium scattering machines, the ones with fixed source-detector angle and the ones where source arm and detector arm can be moved independently. In the second case an elastic scattering spectrum can be measured by either moving the detector- or the source arm, or by using both. In this case also the out-of plane scattering events can be measured. The machines with a fixed geometry usually measure the angular distribution by rotating the sample and scanning through all the possible angles.

2.6.1. Interaction Potential between the Probe Atom and the Sample

Quite naturally in scattering processes, the potential between the probe atom and the sample is essential. It determines not only the elastic scattering peaks via the included corrugation function, but also the height of the peaks and the appearence of additional features in the elastic spectrum. In general, the interaction potential $V(\mathbf{r})$ can be written as

$$V(\mathbf{r}) = \sum_{\mathbf{G}} V_{\mathbf{G}}(z) exp(i\mathbf{G} \cdot \mathbf{R}) \tag{2.20}$$

with $\mathbf{R}$ a vector parallel to the surface and z being the distance from the surface[4]. The exponential term in 2.20 guarantees periodicity and the functions $V_{\mathbf{G}}(z)$ define the "real" interaction. All the functions with $\mathbf{G} \neq 0$ are assumed to be a simple exponential

$$V_{\mathbf{G}}(z) = V_{\mathbf{G}} e^{-\beta_{\mathbf{G}} z} \tag{2.21}$$

with $\beta_{\mathbf{G}}$ being some coefficient, and the single remaining function of interest is $V_{\mathbf{0}}$, the lateral average interaction potential. Qualitatively the interaction of a helium atom approaching at a surface is easy. The potential exhibits a strong, short-ranged repulsive part to account for the reflection and the scattering. But as in all the other particle-particle interaction potentials, an attractive part has to be included to consider the van der Waals interaction.

The short ranged repulsive part originates from the Pauli repulsion in between the closed helium shells and the electrons of the surface. It can usually be described with an exponential term[29]

$$V_{\text{repul}} = C \; exp(-\beta_C z) \tag{2.22}$$

with C and β_C being material specific constants.

The long ranged attractive part is more complicated. At large distances, the attractive part in the nonrelativistic limit reduces to[23]

$$V_{\mathrm{attr}} \;=\; -C_3/z^3. \tag{2.23}$$

While C_3 is given by the Lifshitz formula[4]

$$C_3 \;=\; \frac{\hbar}{4\pi}\int_0^\infty du \frac{\epsilon(iu) \;-\; 1}{\epsilon(iu) \;+\; 1}\alpha_{He}(iu) \tag{2.24}$$

with ϵ being the dielectric function of the material and α_{He} the polarizability of the helium atom.
The overall potential was most of the time approximated by a simple Morse potential

$$V_0(z) \;=\; D\left(e^{-2\beta z} \;-\; 2e^{-\beta z}\right). \tag{2.25}$$

While this function yields analytical bound state energies very easily, which will be of interest later, it does not describe the long range attractive potential correctly. A better description of both the attractive part and the bound states is given by the 3-9 potential of Cole and Tsong[30]

$$V(z) \;=\; \left(3^{3/2}\frac{D}{2}\right)\left[\left(\frac{\sigma}{z}\right)^9 \;-\; \left(\frac{\sigma}{z}\right)^3\right]. \tag{2.26}$$

Here, D denotes the well depth, σ is the distance where the potential vanishes and $z \;=\; 3^{1/6}\sigma$ is the equilibrium position of a bound atom. The potential is plotted in figure 2.9.

This potential does not only describe the long range attractive potential in a better way than the Morse potential, it also has a very simple eigenvalue spectrum.

$$E_n \;=\; -D\left[1 \;-\; \frac{\pi\hbar}{3.07}\frac{n \;+\; \frac{1}{2}}{\sigma\sqrt{2mD}}\right]^6 \tag{2.27}$$

Here, E_n denotes the bound state energy of the probe atoms with mass m in the bound state with quantum number n.

The Beeby Correction

The attractive part in the interaction potential described by 2.26 has numerous consequences. Since the atomic displacement due to thermal phonons is very fast and the helium atoms are very big and slow, the details of the interaction potential are not important and the atom travels through an averaged potential. Within this potential

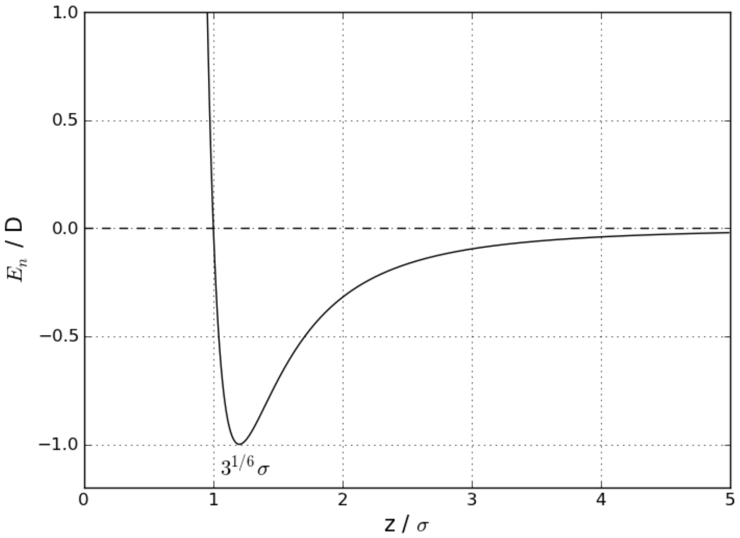

Figure 2.9.: Shape of the 3-9 Potential given in equation 2.26.

the atoms are accelerated by the long range attractive part which gives rise to a higher effective particle energy $E_{iz\ eff}$ and a reduced effective angle of incidence θ_i.

$$\begin{aligned} E_{iz\ eff} &= E_{iz} + D \\ \sin\theta_i' &= \frac{\sin\theta_i}{\sqrt{1 + \frac{D}{E_i}}} \ .^1 \end{aligned} \tag{2.28}$$

The R-dependence of V(z)

In all these approximations the atom-surface potential is assumed to be constant for every $\mathbf{R}$ at the same distance z from the surface. In general, the effective turning point and thus the overall potential changes with the lateral position of the impact within the surface unit cell. Figure 2.10 displays this effect for the positions A and B, one being at an atom position and one being in between atomic positions. In helium atom scattering experiments this has practically no effect since the helium atoms are too large and too slow compared to the atomic vibrations. The periodic change of the local potential eigenvalues on the other hand has an effect on the width of resonance features as explained in section 2.6.3.

2.6.2. Elastic Peaks and Surface Corrugation

By using Braggs law and the knowledge about the wave-particle dualism the angles of the elastic scattering peaks can be easily calculated. But the measured elastic peaks

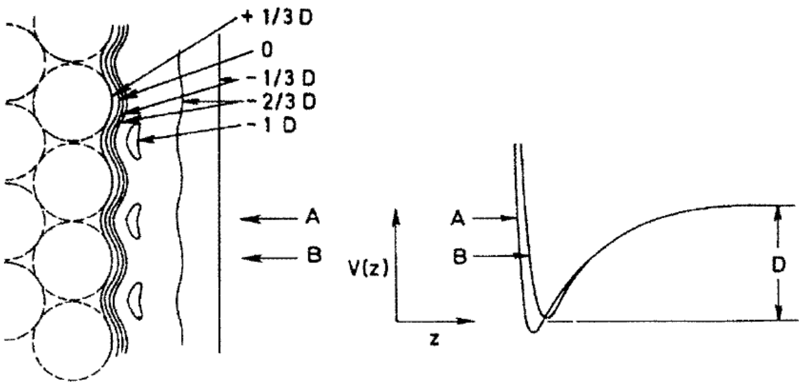

Figure 2.10.: Interaction potential equipotential lines for an ordered surface in terms of the potential depth D. Dependence of the effective potential on the relative position A or B. From Farias & Rieder 1998[1]

also exhibit additional information, mainly due to their height and their broadness. The latter mainly depends on the energy distribution of the incoming helium beam and is thus given by the experimental parameters. The height of the peaks on the other hand depends on the roughness, or corrugation of the sample. As explained before, in helium atom scattering, the probe atoms are not reflected by the nuclei, but from the electron density a few Angstrom above the surface. This is the reason why in ionic crystals, where the charges are firmly bound to the nuclei, the corrugation and thus the elastic scattering peaks are high. On metallic surfaces on the other hand, the electron density corrugation is completely flat, since a corrugation would lead to high electrostatic fields and a resulting current. Here one can not observe any elastic scattering peaks.[31]
Since there is a clear correlation between those two variables, there has been great effort in trying to link them in order to be able to calculate the surface corrugation from the measured elastic peak intensities. This section of this work briefly describes the two mainly used approximative methods[1] and introduces a third one used in this work.

The Hard Corrugated Wall Model

Almost every approximative method to solve the corrugation-scattering problem uses the hard corrugated wall model. The general interaction potential $V(\mathbf{R}, z)$ with $\mathbf{R}$ being a position vector parallel to the surface and z being the distance from the surface is at first assumed as a product $\xi(\mathbf{R})V(z)$ with $\xi(\mathbf{R})$ being the surface corrugation and $V(z)$ the probe-surface interaction potential. In this approach, the attractive part of the probe-sample interaction potential is neglected and the repulsive part is infinite and introduced instantaneuos at the surface, thus, introducing a hard wall.

$$V(z) = \begin{cases} 0 & \text{for } z > 0 \\ \infty & \text{for } z \leq 0 \end{cases} \tag{2.29}$$

All of the presented approximative methods also depend on the Rayleigh assumption. It declares that both the incoming and the outgoing particles can be considered as plane waves up to the surface of the sample.

$$\Psi(\mathbf{R}, z) = exp[i(\mathbf{K} \cdot \mathbf{R} + k_{iz} z)] + \sum_{\mathbf{G}} A_G exp\{i[(\mathbf{K} + \mathbf{G}) \cdot \mathbf{R} + k_{Gz} z]\} \tag{2.30}$$

with the incoming wavevectors $k_i = (\mathbf{K}, k_{iz})$, the outgoing ones $k_G = (\mathbf{K}_G, k_{Gz})$ and the scattering amplitudes A_G. Applying the hard wall approximation, the wavefunction must vanish at the surface due to the infinite potential $\Psi[\mathbf{R}, z = \xi(\mathbf{R})] = 0$, hence one obtains:

$$\sum_{\mathbf{G}} A_G exp\{i[\mathbf{G} \cdot \mathbf{R} + k_{Gz} \xi(\mathbf{R})]\} = -exp[ik_{iz} \xi(\mathbf{R})] \tag{2.31}$$

The GR-Method

By multiplying each side of equation 2.31 with $exp[-ik_{iz}\xi(\mathbf{R})]$, one obtains the matrix equation

$$\sum_{\mathbf{G}} A_{\mathbf{G}} M_{\mathbf{GR}} = -1 \tag{2.32}$$

with

$$M_{\mathbf{GR}} = exp\{i[(k_{Gz} - k_{iz})\xi(\mathbf{R}) + \mathbf{G} \cdot \mathbf{R}] \tag{2.33}$$

Equation 2.32 has to be fulfilled for every **G** and **R** considered. Therefore one chooses the **R** and **G** vectors in a way that they are uniformly distributed over the unit cells in real and reciprocal space respectively and calculates a quadratic matrix $M_{\mathbf{GR}}$. This gives rise to a simple system of linear equations that can be efficiently solved by matrix inversion, as long as $|M_{\mathbf{GR}}| \neq 0$. This last condition is fulfilled as long as only **R** vectors within the first unit cell are chosen[32]. The calculated $A_{\mathbf{G}}$'s relate to the scattered intensities with:

$$P_{\mathbf{G}} = \frac{|k_{Gz}|}{|k_{iz}|} A_{\mathbf{G}} A^*_{\mathbf{G}} \rightarrow \sum_{\mathbf{G}} P_{\mathbf{G}} = 1 \tag{2.34}$$

The calculated $P_{\mathbf{G}}$'s are the expected elastic scattering intensities for the assumed corrugation $\xi(\mathbf{R})$. The **GR**-Method delivers convergent solutions as long as the relative corrugation, $\beta_0 = \frac{\xi_{\max}}{a}$ is smaller than 18%[1].

The Eikonal Approximation

If one multiplies equation 2.31 with $exp\{-i[\mathbf{G}' \cdot \mathbf{R} \ + \ k_{G'z}\xi(\mathbf{R})]\}$ and integrates over the unit cell, one obtains the matrix equation

$$\sum_{\mathbf{G}} M_{\mathbf{G}'\mathbf{G}} A_{\mathbf{G}} \ = \ A^0_{\mathbf{G}'} \tag{2.35}$$

whereas

$$M_{\mathbf{G}'\mathbf{G}} \ = \ \frac{1}{S} \int_{\text{u.c.}} exp\{i[(\mathbf{G} \ - \ \mathbf{G}') \cdot \mathbf{R} \ + \ (k_{Gz} \ - \ k_{G'z})\xi(\mathbf{R})]\} d\mathbf{R} \tag{2.36}$$

and

$$A^0_{\mathbf{G}'} \ = \ -\frac{1}{S} \int_{\text{u.c.}} exp\{-i[\mathbf{G}' \cdot \mathbf{R} \ + \ (k_{G'z} \ - \ k_{iz})\xi(\mathbf{R})]\} d\mathbf{R} \tag{2.37}$$

where S denotes the unit cell area[1]. In cases where $\beta_0 \ \leq \ 10\%$, the matrix $M_{\mathbf{G}'\mathbf{G}}$ reduces approximately to unity and thus

$$A_{\mathbf{G}} \ = \ A^0_{\mathbf{G}'} \tag{2.38}$$

One just has to integrate equation 2.37 to calculate the expected intensities[33]. The eikonal approximation additionally produces problems in unit cells with mirror symmetry. Here it can not be distinguished if the calculated $\xi(\mathbf{R})$ or $-\xi(\mathbf{R})$ corresponds to the correct solution and it has to be checked with some other method[1].

The Inversion Problem

One is usually interested in calculating the surface corrugation $\xi(\mathbf{R})$ from the measured intensities $P_{\mathbf{G}}$. This represents an inversion problem and can not be solved in an easy way. The usual approach is to approximate the surface corrugation using a sum of two dimensional cosine functions and optimizing the parameters till the calculated intensities fit the measured intensities as well as possible.

However, there is another way to reach a sufficiently close approximation to the real surface corrugation without modeling the surface using cosines. In this approach, one calculates the corrugation iteratively using the Rayleigh approximation 2.31.

A starting corrugation can be calculated using

$$\xi^0(\mathbf{R}) \ = \ \frac{1}{|k_i| \cos\theta_i} \cdot \arccos\left[-\frac{1}{\sqrt{P_0} \ + \ 1} \sum_{\mathbf{G}'} \sqrt{P_{\mathbf{G}'} \frac{\cos\theta_i}{\cos(\theta_{SD} \ - \ \theta_i)}} \cdot \cos\left(\mathbf{G}' \cdot \mathbf{R}\right) \right] \tag{2.39}$$

while setting the indefinite values to an arbitrary value near the real value and iterating the corrugation using

$$\begin{aligned}\xi^n(\mathbf{R}) = \frac{1}{|k_i|\cos\theta_i} \cdot \arccos\Bigg[-\frac{1}{\sqrt{P_0}+1}\sum_{\mathbf{G'}}\sqrt{P_{\mathbf{G'}}\frac{\cos\theta_i}{\cos(\theta_{SD}-\theta_i)}} \cdot \cdots \\ \cdots \cos\left(\mathbf{G'}\cdot\mathbf{R} + |k_i|\cdot\cos(\theta_{SD}-\theta_i)\cdot\xi^{n-1}(\mathbf{R})\right)\Bigg]\end{aligned} \quad (2.40)$$

The P_0 appearing in these equations is the specular peak intensity. The complete derivation of this iteration rule can be found in the appendix.

2.6.3. Surface Resonances

In this section a special effect of inelastic scattering is viewed in greater detail. As already explained in section 2.6, inelastic scattering from surfaces occurs when a helium atom is scattered from the surface while interacting with a surface phonon. In this case equations 2.18 and 2.19 hold. The inelastically scattered helium atoms contribute to the inelastic background signal in an elastic scattering measurement and produce a more or less homogeneous background as can be seen in figure 2.11.

The momentum $\mathbf{Q}$ of the interacting phonon defines the angle at which the helium atom will leave the surface. It is calculated very easily using equations 2.18 and 2.19

$$|\mathbf{Q}| \;=\; \sqrt{k_i^2 \pm \Delta E\frac{2m}{\hbar^2}}\sin(\Theta_f) \;-\; k_i\sin(\Theta_i) \quad (2.41)$$

which requires that the energy of the phonon is known. Since most of the time the dispersion of the surface phonons is unknown, the energy has to be measured using a time of flight measurement beforehand.[27]

However, in most elastic spectra little features appear in between the elastic scattering peaks. Sometimes these features are just small and broad variations of the background intensity, sometimes large and sharp peaks appear. In general, two important processes cause such features.

The first one is a kinematical focussing effect, that arises when the so-called scan curve (here for a fixed-angle geometry with the source-detector angle Θ_{SD})

$$\Delta E(\mathbf{Q}) \;=\; \frac{\hbar^2}{2m}\left(\frac{(k_i\sin(\Theta_i)+Q)^2}{\sin^2(\Theta_{SD}-\Theta_i)} \;-\; k_i^2\right) \quad (2.42)$$

is tangent to a surface phonon dispersion. At this special angle a lot of possible phonon modes contribute to the inelastic background intensity, which consequently rises. Kinematical focussing peaks are easily identified by their special shape. Figure 2.12 illustrates the origin of the kinematical focussing effect. In figure 2.12a, the scan curve intersects the phonon dispersion, enabling the participation of many phonons to the signal. Figure

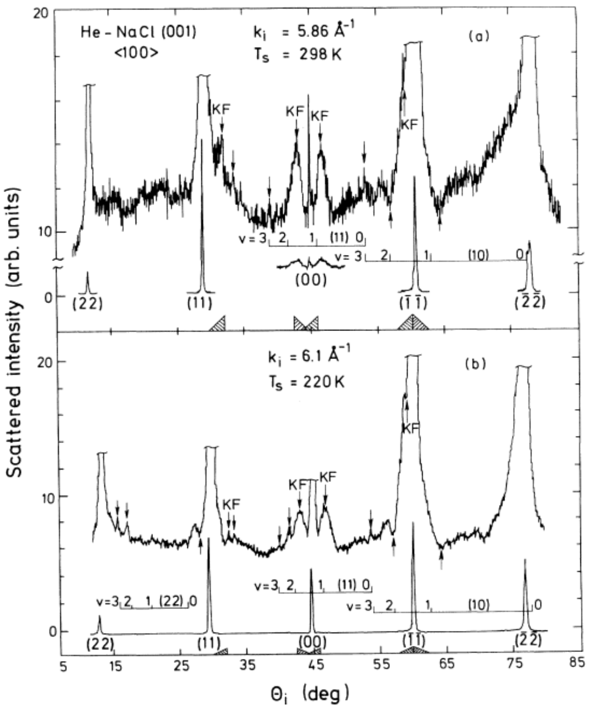

Figure 2.11.: Elastic HAS spectra of NaCl <100> at different temperatures, showing the widely homogeneous background signal with various kinematical focussing features. From Benedek 1983[34]

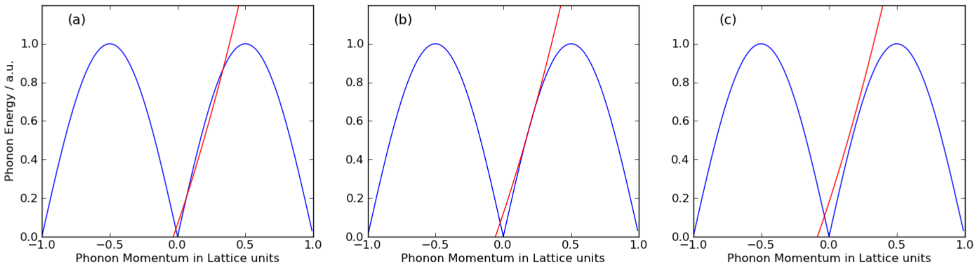

Figure 2.12.: Illustration of the origin of kinematical focussing effects. (a) The scan curve cuts the dispersion twice. The scattered intensity is slightly enhanced. (b) The scan curve is tangent to the dispersion. A maximum of phonon modes contribute to the scattered intensity, yielding a peak. This is known as the kinematical focussing effect. (c) The scan curve cuts the dispersion once, the scattered intensity suddenly falls back to a normal value.

2.12b shows the case at the peak of the feature. The scan curve is now tangent to the dispersion and a maximum of phonons participate to the background signal at that position. If the angle is increased further, the case shown in figure 2.12c occurs. The scan curve then misses the dispersion and the enhancement of the background signal rapidly vanishes. This gives rise to a slowly arising peak that sharply vanishes, producing a significant triangular shape.

The other, more interesting effect is the so-called elastic surface resonance. Those resonances arise from a more complex behavior of the scattering process and require a more realistic treatment of the surface. As explained in section 2.6.2, if the surface is assumed to be a hard corrugated wall, an incoming helium atom has two possibilities. It can either scatter elastically by interacting with a surface **G**-vector, yielding the elastic scattering peaks, or to scatter inelastically interacting not only with a **G**-vector but also with a surface phonon. If an interaction potential like the 3-9 Potential in section 2.6.1 is introduced, conservation of energy suddenly allows additional channels. If the interaction potential possesses bound states, the incoming atom does not only have the listed possibilities, but can also interact with every **G**-vector to reach a bound state at the surface.

It is very important to understand the occurrence of the elastic resonance features in the elastic spectrum. The two most important processes for the appearence of elastic resonance features are (C) and (D) in figure 2.13. Case (C) illustrates the inelastic scattering by interacting with a surface phonon and a possible surface lattice vector:

$$\begin{aligned} \mathbf{K_i} + \mathbf{Q} \pm \mathbf{G} &= \mathbf{K_f} \\ \mathbf{k_i}^2 \pm E(\mathbf{Q}) &= \mathbf{k_f}^2 \end{aligned} \tag{2.43}$$

Case (D) illustrates a somewhat more complicated procedure. In elastic resonant scattering the helium atom enters the bound state elastically. In this case the new scattering channel opens, if

$$\mathbf{K_i} \pm \mathbf{G} = \mathbf{K_f} \tag{2.44}$$

$$\mathbf{k_i}^2 = \left(\mathbf{K_i} + \mathbf{G}_{\|}\right)^2 + \mathbf{G}_{\perp}^2 - \frac{2m}{\hbar^2}\left|\epsilon_n\right| \tag{2.45}$$

where ϵ_n is the bound state energy and $\mathbf{G}_{\|}$ and $\mathbf{G}_{\perp}$ the parallel and perpendicular components of the **G**-vector to the plane of incidence. Or, if in equation 2.45 only **G**-vectors parallel to the angle of incidence are considered,

$$\mathbf{k_i}^2 = (\mathbf{K_i} + \mathbf{G})^2 - \frac{2m}{\hbar^2}\left|\epsilon_n\right| \tag{2.46}$$

This formula for the conservation of energy does not explain what happens in detail. The incoming helium atom with $\mathbf{K_i}$ and $\mathbf{k_{iz}}$ interacts with a surface **G**-vector in such a

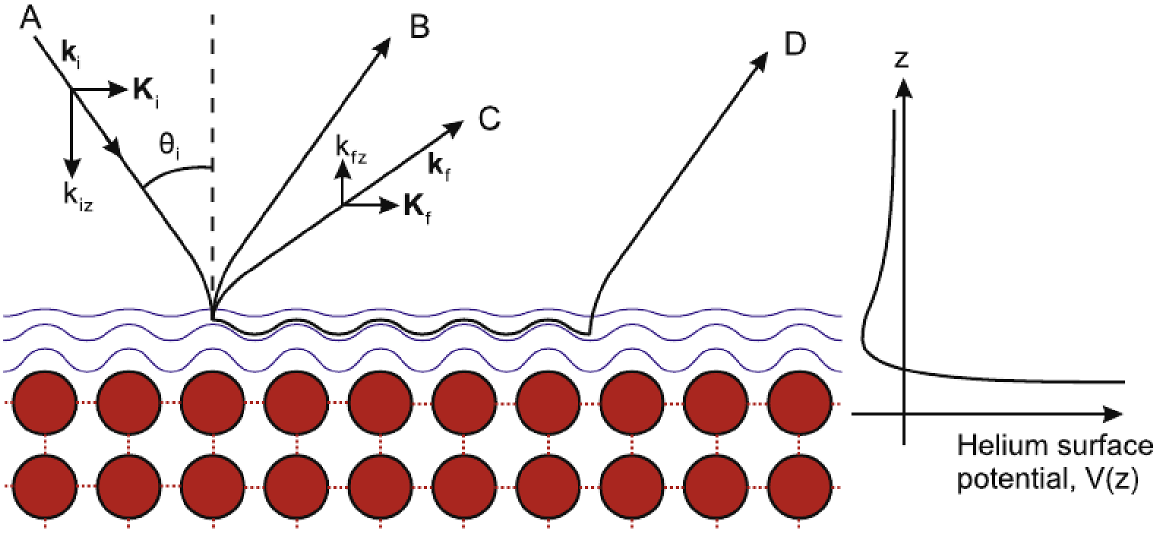

Figure 2.13.: Illustration of the different possibilities of diffraction. The incloming beam (A) can be scattered elastically (B), inelastically by interacting with a Phonon (C) or can be temporarily trapped in a bound surface state (D). From Jardine, 2009[35]

way that the energy of the particle in parallel movement to the surface is increased

$$\mathbf{K_i}^2 \;\rightarrow\; (\mathbf{K_i} \;+\; \mathbf{G})^2 \tag{2.47}$$

while at the same time the conservation of energy forces the perpendicular energy in $\mathbf{k_{iz}}$ to decrease. If this condition is fulfilled for

$$\mathbf{k_{iz}}^2 \;\rightarrow\; -\frac{2m}{\hbar^2}\,|\epsilon_n| \tag{2.48}$$

with ϵ_n being an energy eigenstate of the atom-surface interaction potential, the atom is thereby bound to this surface state.

The atom can move freely along the surface until another scattering event takes place. This is illustrated in figure 2.14. The atom can leave the bound state by interacting with a $\mathbf{G}$-vector and / or a phonon. If it leaves the surface purely elastically by only interacting with the reciprocal surface vector $\mathbf{G}'$, the whole condition reads as:

$$\mathbf{k_i}^2 \;=\; (\mathbf{K_i} \;+\; \mathbf{G})^2 \;-\; \frac{2m}{\hbar^2}\,|\epsilon_n| \;=\; (\mathbf{K_i} \;+\; \mathbf{G}')^2 \;-\; \frac{2m}{\hbar^2}\,|\epsilon_n| \;=\; \mathbf{k_f}^2 \tag{2.49}$$

Since the parallel momentum difference is just $\mathbf{G} \;-\; \mathbf{G}'$,

$$\mathbf{K_f} \;=\; \mathbf{K_i} \;+\; \mathbf{G} \;-\; \mathbf{G}' \tag{2.50}$$

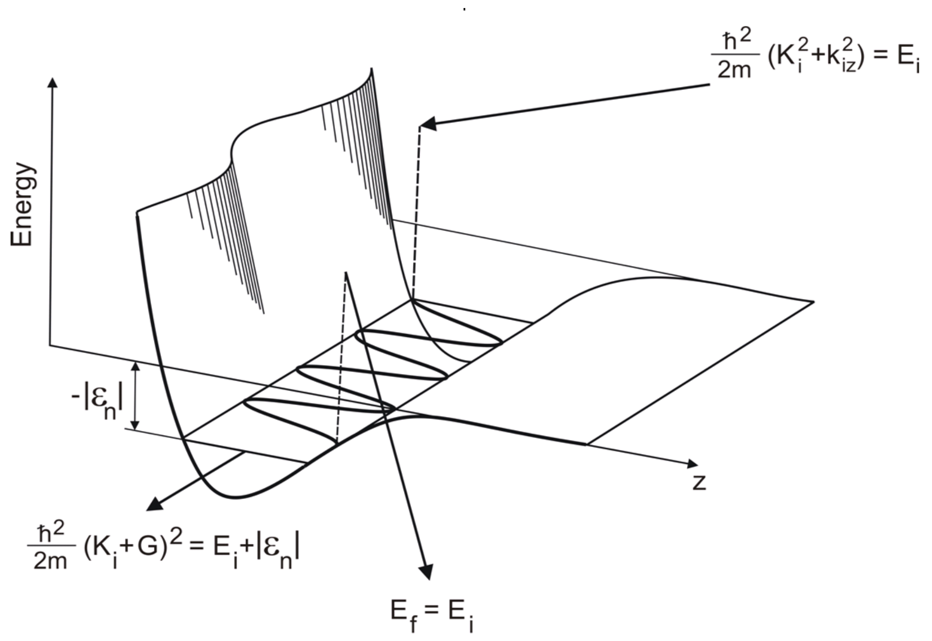

Figure 2.14.: Illustration of the helium-surface interaction potential along the path of a bound atom. An atom can enter a bound state of the interaction potential and travel along the corrugated surface if equation 2.45 is fulfilled. From Benedek & Toennies 2011[36]

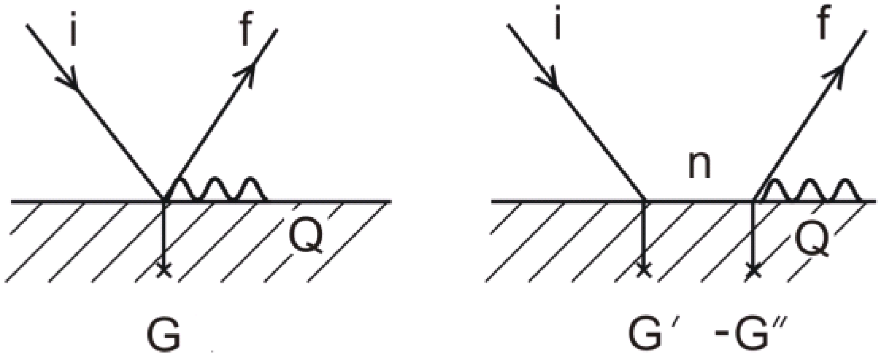

Figure 2.15.: Schematic illustration of an inelastic scattering process and a resonant scattering process with identical outcome. From Benedek & Toennies 2011[36]

the angle of the outgoing helium particle must correspond to an elastically scattered atom. In the case of purely elastic adsorption and desorption, the only measurable difference at the resonance condition is the change of the relative intensities of the elastic scattering peaks. If on the other hand inelastic interaction with a phonon is taken into account, the case is by far more interesting. In this case just elastic adsorption is considered again, while the desorption process is considered to be inelastic. This means that the conditions for the atom to transit into the bound state remains unchanged, while the kinematic condition for the parallel momentum is altered to

$$\mathbf{K_f} \;=\; \mathbf{K_i} \;+\; \mathbf{G} \;-\; \mathbf{G}' \;+\; \mathbf{Q} \tag{2.51}$$

Thus, only the angle at which the helium atom leaves the surface is affected by the properties of the phonon. Since there are phonons with every momentum available, the outgoing helium atom can contribute to the background signal at any angle and it is indistinguishable from the directly scattered ones.

The careful reader may ask how the resonance process can be of any interest if the outcome of this process is indistinguishable from the process that also occurs without the possibility of the bound state. But this is exactly the interesting point. Everywhere in nature, when two different paths of events give rise to an indistinguishable outcome, interference occurs. By interacting with the surface and, especially interacting with the surface phonon, the quantum-mechanical phase of the helium atom is altered and differs from the phase of the directly scattered helium[37]. As a consequence, those two wavefunctions interfere either constructively, yielding a peak in the background signal, or destructively, producing a dip in it. The size and shape of those resonant features are studied in Celli's paper[37] and will not be further discussed here.

In order to measure the resonance effects, the resonance condition 2.45 has to be

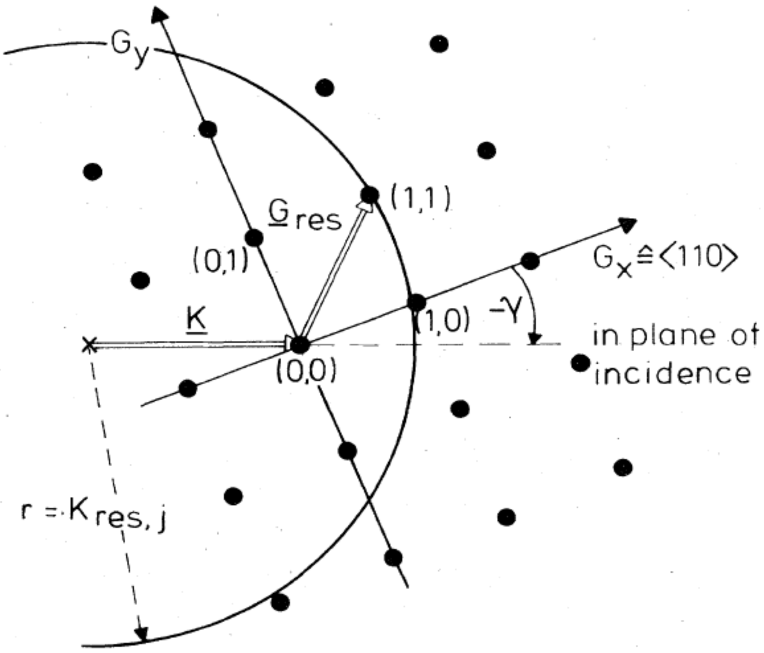

Figure 2.16.: Constructive approach to illustrate the resonance condition 2.45. Every time the energy circle hits a reciprocal lattice point, resonance processes are possible. From Hoinkes 1980[3]

fulfilled. According to Hoinkes[3] this can be done in three different ways (see figure 2.16):

- Variation of the azimuthal angle γ at fixed E_i and Θ_i by rotating the sample around its surface normal. This corresponds to changing the respective size of $\mathbf{G}_\perp$ and $\mathbf{G}_\parallel$, while keeping $\mathbf{G}^2 = \mathbf{G}_\parallel^2 + \mathbf{G}_\perp^2$ constant, since the surface lattice vectors will just change their orientation. The resonance condition is fulfilled, when one of the $\mathbf{G}$ vectors hits the $\mathbf{k_i}$-circle. This kind of measurement is the most popular for measuring the bound state resonances, since the peaks produced are very sharp[3].
- Variation of the incident angle Θ_i while keeping γ and E_i constant, as it is done in standard elastic measurements. This changes the length of the parallel momentum $\mathbf{K_i} = |\mathbf{k_i}| sin(\Theta_i)$ along the surface and therefore shifts the circle in figure 2.16. This method is very convenient, since the elastic measurements of structural determination experiments can be analyzed.
- Variation of the incident Energy E_i by changing the nozzle Temperature T_N, while keeping Θ_i and γ fixed. This corresponds to changing the length of $\mathbf{K_i}$, as in the previous example, while simultaniously changing the radius of the circle. This kind of experiment is usually performed at the incident angle of the specular peak, since this position provides the best signal to noise ratio.

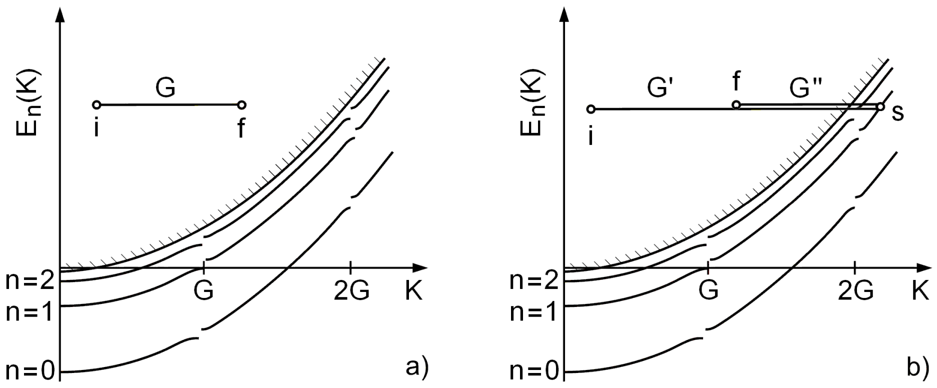

Figure 2.17.: Cellis diagrams to show the elastic scattering (a) process and the elastic scattering via the bound state resonance (b). Every point corresponds to an energy of the helium atoms. The bound states along the surface show band structure effects due to the periodic variation of the ineraction potential. From Benedek & Toennies 2011[36]

Bound State Dispersion

All of the considerations up to now assumed the atom-surface interaction potential to be representable as a simple product of the surface corrugation function $\xi(\mathbf{R})$ and the perpendicular interaction $V(z)$. As explained before and illustrated in figure 2.10, the perpendicular interaction potential depends on the lateral impact position of the helium atom within the surface unit cell. This means in particular, that the potential varies periodically along the path of a bound atom. Classically speaking, the total energy of the atom, bound to the surface and moving with the momentum $\mathbf{K}$ would be

$$E_n(\mathbf{K}) = \frac{\hbar^2 K^2}{2m} - |\epsilon_n| \tag{2.52}$$

thus, just a shifted parabola. But since there is a periodicity in the potential and thus a corresponding $\mathbf{G}$-vector, this dispersion is also altered by band structure effects, mainly the appearence of gaps and a shift of the energies close to the unit cell boundary[37]. These alterations especially affect the bound state with the lowest energy, since a small variation on the potential well depth gives rise to large variation in the energy.

Due to the fact that in a helium beam apparatus there is some variability in the energies and the angles of the incoming helium atoms, the helium atoms do not hit the surface at the same spot. Combined with Celli's dispersion[37], this yields a high variability in the case of a resonantly scattered atom. The interaction potential measured by scattering experiments is thus only an averaged one.

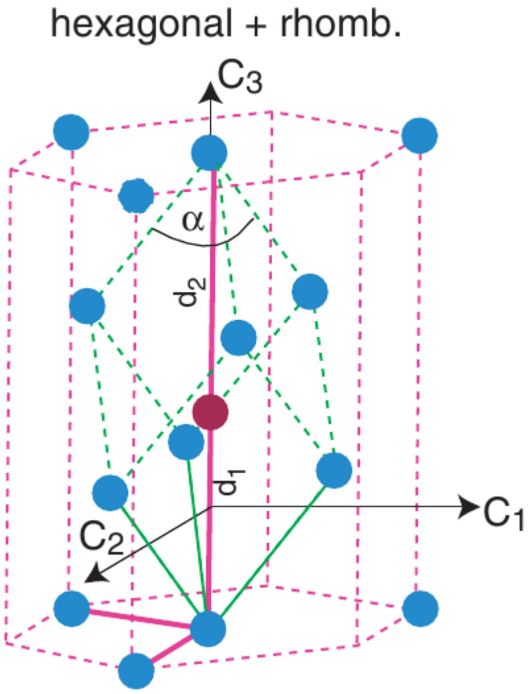

Figure 2.18.: Three dimensional structure of bismuth with the hexagonal and the rhombohedral unit cell. From Hofmann 2006[14]

2.7. Structure and Properties of the Bi(111) surface

Bismuth, like most group V semimetals, crystallizes in a rhombohedral symmetry. Every atom has three nearest neighbours and three next nearest neighbours that are just slightly further away. The so-called "arsenic" A7 structure has two atoms per unit cell. The vectors spanning the unit cell enclose an angle of 57.35°and the distance ratio for the second atom is $\frac{d_1}{d_2} = 0.88$ with d_1 and d_2 as labeled in figure 2.18. The Bi(111) plane is the most important surface of bismuth for technical applications, since it is its natural cleavage plane and thus cheap and easily available. It additionally turns out to be the preferred direction for epitaxial growth. Figure 2.19 displays two different views of the Bi(111) surface. As indicated there, bismuth crystallizes in a bilayer structure. Within those bilayers, the atoms are thightly bonded by covalent bonds. In between those bilayers, the bonding is weak and van-der Waals like and can easily be broken. This is the main reason why the (111) plane is the natural cleavage of bismuth.[14]

The surfaces of bismuth are particularly well suited for an investigation with helium atom scattering since their properties differ subtantially from the bulk. For example, the bismuth surfaces are far better metals than the bulk, and every method compared to HAS measures also a lot of bulk values as explained before. There have been a lot of

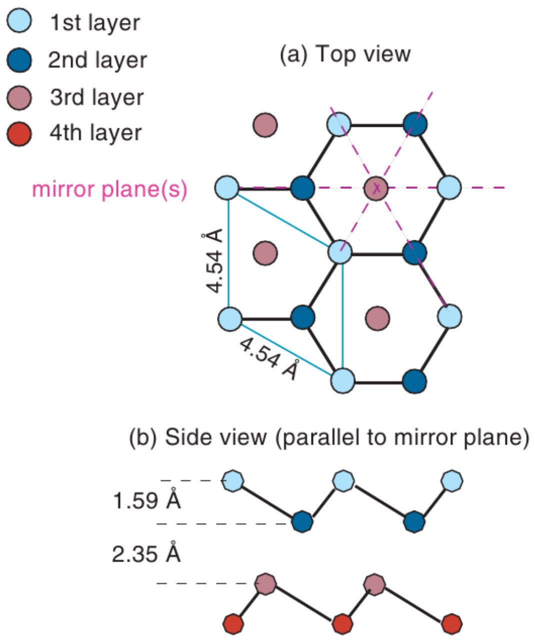

Figure 2.19.: Structure of the Bi(111) surface. (a) Top view of the first three atomic layers. The light blue circles denote the top layer nuclei. (b) Side view of the surface. Bismuth crystallizes in a bilayer structure perpendicular to the [111] direction. From Hofmann 2006[14]

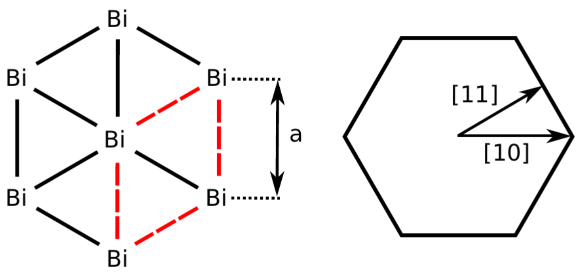

Figure 2.20.: Structure of the Bi(111) top surface layer with the two distinguishable directions marked. The dashed red rhombus indicates the unit cell with a distance $a = 4.54$ Å.[38]

measurements to determine the electronic properties of the Bi(111) surface. The most interesting results affect the electron and hole pockets at the surface reported by Ast and Höchst 2001[9]. Those localized charge densities could account for an electron density surface corrugation that would otherwise not be expected on a metallic surface.

The only two distinguishable directions on the surface are the <11> and the <10> direction as sketched in figure 2.20.

3. Experimental Setup

All measurements used in this work were performed on the HANS[1] helium atom scattering machine. As illustrated in figure 3.1, the source-detector angle of the machine is fixed at $\Theta_{SD} = 91.5°$. The elastic scattering spectra can be measured by rotating the sample, thus changing the angle of incidence at the same time as changing the angle of the outgoing atoms.

A nearly monoenergetic beam of helium atoms is produced in the supersonic gas expansion nozzle ((1) in figure 3.1). The temperature of the nozzle can be varied using a coldhead between 70 K and room temperature, corresponding to an energy range from 15.1 to 64.6 meV. The higher energies are practically not accessible, since the beam intensity falls with rising temperature proportional to $\frac{1}{\sqrt{T}}$.[27]

In the main chamber the helium beam hits the sample and is diffracted. The sample can be rotated and its temperature varied between 123 and 900 K. Its surface is furthermore cleaned by sputtering using an argon ion gun ((7) in figure 3.1) and annealing at 423 K.

---

[1] Helium Atom Nondestructive Scattering

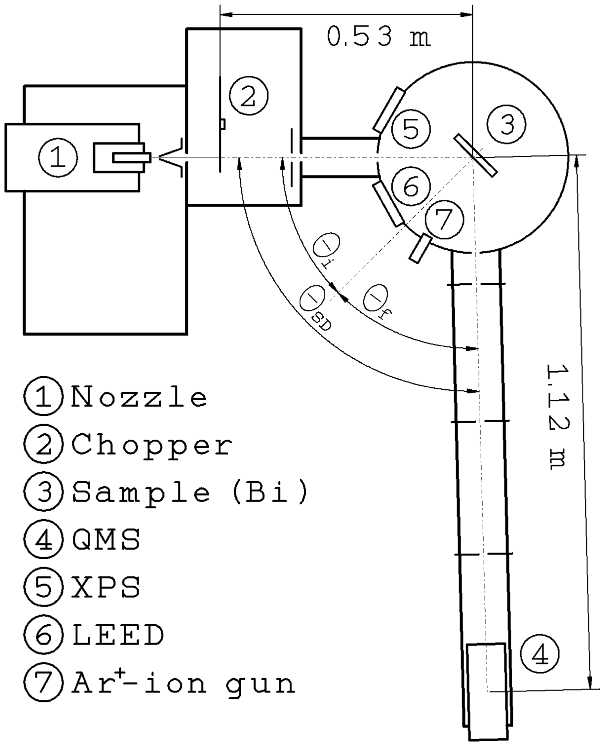

Figure 3.1.: Illustration of the HANS helium atom scattering apparatus. The source-detector angle Θ_{SD} is 91.5°. From Tamtögl et al 2010,[39].

4. Measurements and analysis

4.1. Elastic HAS Measurements on Bi(111)

Elastic spectra of the Bi(111) surface were recorded using helium atom scattering at several incident energies. The two most significant measurements are presented here, other measurements were mostly used to check the predictions made by the measured results.

Figures 4.1 and 4.2 display two elastic scattering spectra for measuring two qualitatively different entities. The intensities of the peaks in those two measurements differ because the HAS apparatus was recalibrated. While the measurement displayed in figure 4.1 shows some higher fluctuation in the background signal, it is perfect for measuring the bound state energies, while the measurement in figure 4.2 contains information for the surface corrugation up to the third order.

4.2. Surface Corrugation

Using the measurements presented in figure 4.2, the surface corrugation can be calculated, with different approaches such as the **GR**-method (equation 2.32) or the eikonal approximation (equation 2.37). In this work the straightforward approach of the iterative calculation (equations 2.39 and 2.40) was chosen since it was unclear if the approximations used in previous work[38] were valid for bismuth.

The measurements were taken at a nozzle temperature of 130 K, corresponding to a beam energy of 28 meV. The surface has been cooled down to 118 K to minimize the inelastic background signal.

In this iterative approach the natural asymmetry of the elastic spectrum was ignored and the intensities of the same orders on both sides were averaged, as well as the relative angles with respect to the specular peak. The used data is listed in table 4.1.

The iteration doesn't converge near the core positions and has to be fitted there. Apart from this drawback, the calculated corrugation height corresponds to the one obtained by Mayrhofer et. al.[38] as listed in table 4.2. Figure 4.4 and 4.3 display the calculated corrugation functions by Mayrhofer et al and the current work respectively in three dimensions.

Since the maximum height of the calculated corrugation in the iterative approach is

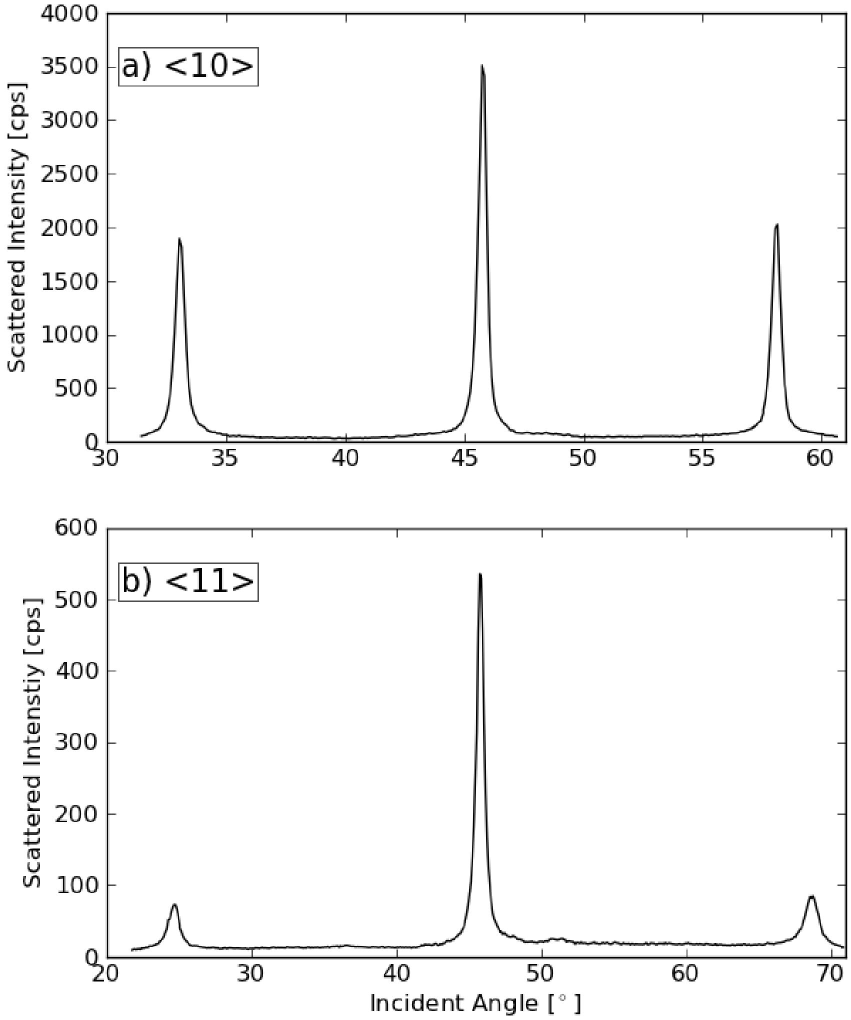

Figure 4.1.: Elastic helium atom scattering spectrum from Bi(111) up to first order at a beam energy of 15.1 meV. (a) The measurement in <10> direction yields high first order peaks. (b) Besides the small first order peaks, there are some additional features to be seen in the <11> direction.

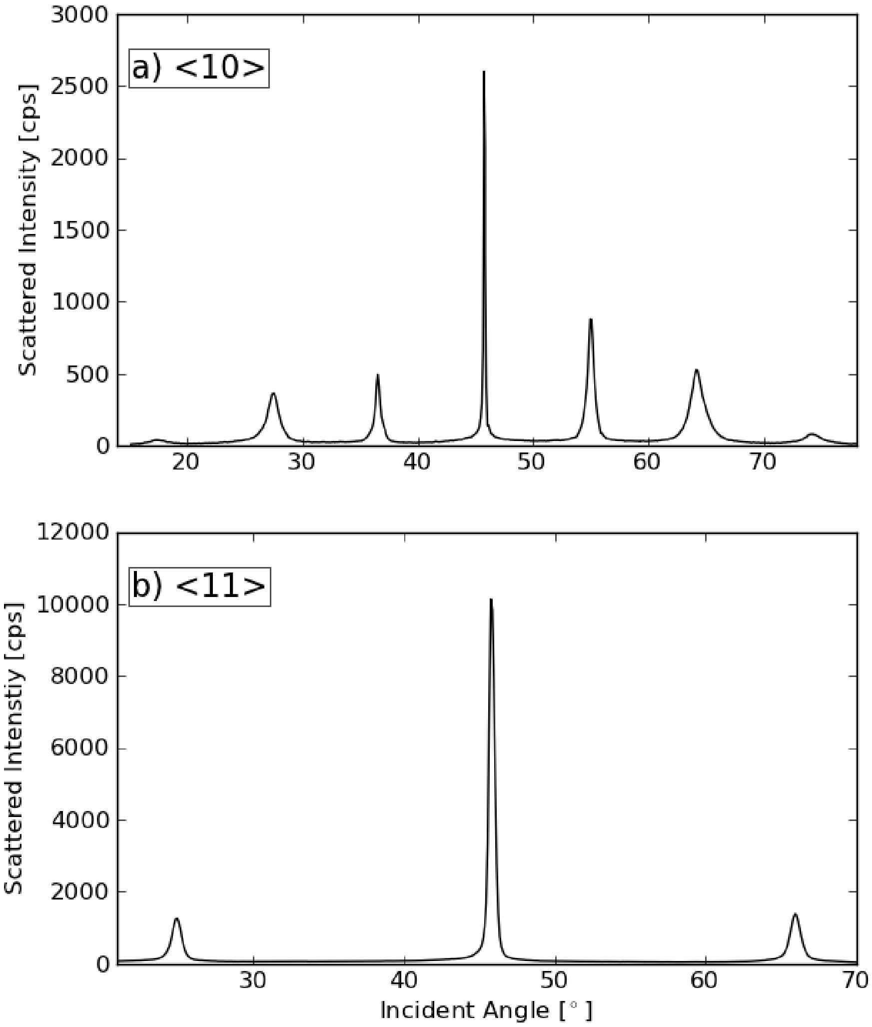

Figure 4.2.: Elastic helium atom scattering spectrum of Bi(111). (a) At a beam energy of 28 meV, third order peaks are measurable in the <10> direction. (b) At a beam energy of 22.6 meV, only the first order peaks in the <11> direction are in the angular range.

Table 4.1.: Scattering data used for the iterative calculation of the surface corrugation taken from the <10> measurement in figure 4.2

order	...	Number of the order of diffraction peak
angle	...	Angle of the diffraction peak relative to the specular in degrees (averaged over both directions)
I	...	Intensity of the diffraction peak (averaged over both directions) in counts per second (cps)

order/#	angle/°	I/cps
0	0.00	2600.0
1	9.24	687.5
2	18.29	446.0
3	28.36	60.5

Table 4.2.: Corrugation heights from different calculations in comparison to the solution of the iterative approach. Data from Mayrhofer et. al.[38]

Method	...	Approximation Method
corr. height	...	Corrugation height calculated in % of the lattice constant a

Method	corr.height / % of a
GR[38]	12.2
Eikonal[38]	12.0
Iterative	16.3

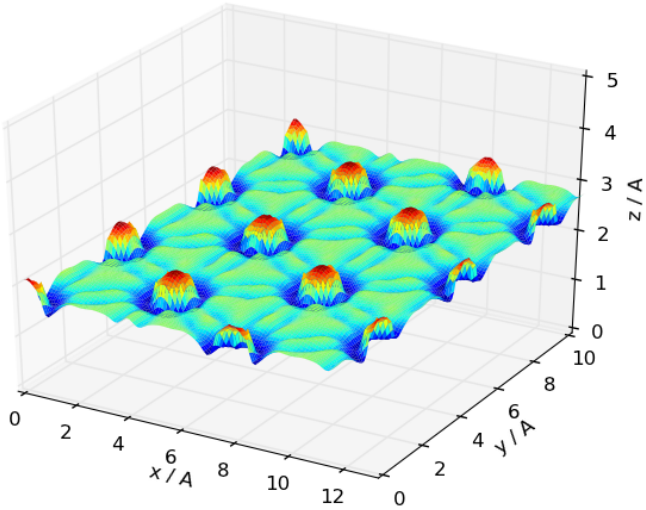

Figure 4.3.: Calculated corrugation function using the iterative approach from equations 2.39 and 2.40

at an interpolated point, the **GR**-method and the eikonal approximation most certainly produce more precise results. Besides the existence of a surface corrugation on a conducting surface without steps, the structure of the surface itself is very interesting. In between the nearest neighbour atoms there seems to be an enhanced electron density. This could point to covalent-like bonds along the surface and will be subject to further investigations.

4.3. Surface Resonances

The measurement of surface resonances is significantly more complicated. The <11> spectrum plotted in figure 4.1 contains a lot of information that is invisible on a larger scale. The measurements were taken at a nozzle temperature of 70 K, corresponding to a beam energy of 15.1 meV, the sample was at room temperature. The enlarged background signal plotted in figure 4.5 shows a lot of fluctuation and some clear features at 51°and 37°. In order to prove that those peaks are resonance features, several peaks have to correspond to the same bound state energy. Since the features are rather broad, this task turns out to be more complicated than expected. Since the bound state energies are unknown, one has to check every angular position at which the resonance is suspected

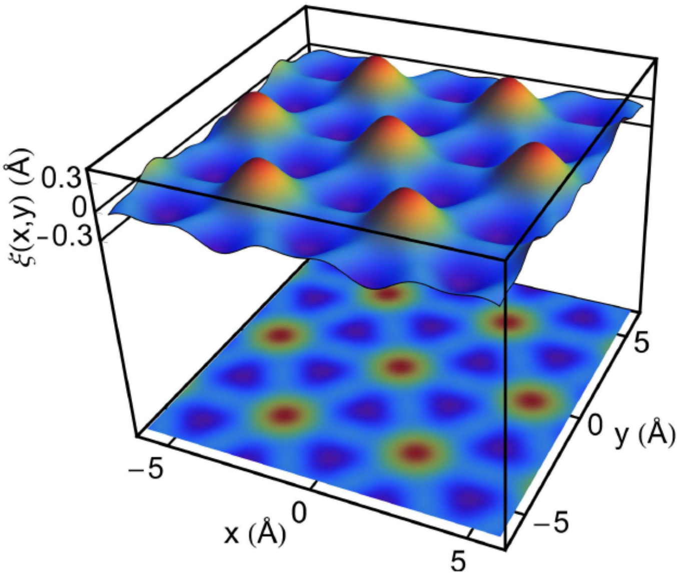

Figure 4.4.: Calculated corrugation function using the eikonal approximation. From Mayrhofer et. al.[38]

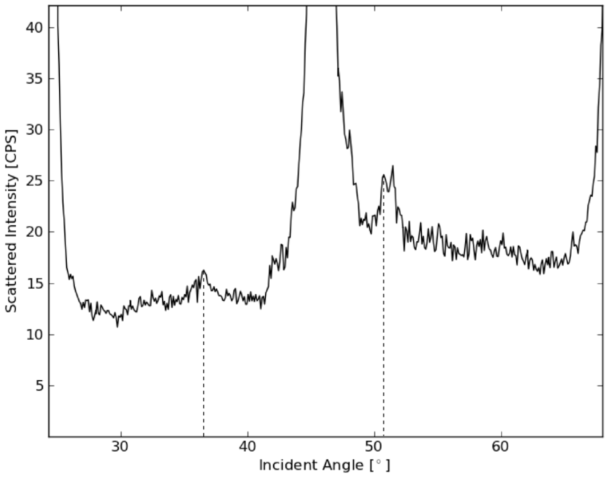

Figure 4.5.: Enlarged part of the <11> measurement in figure 4.1. The features at 51° and 37° are suspected to be resonance peaks.

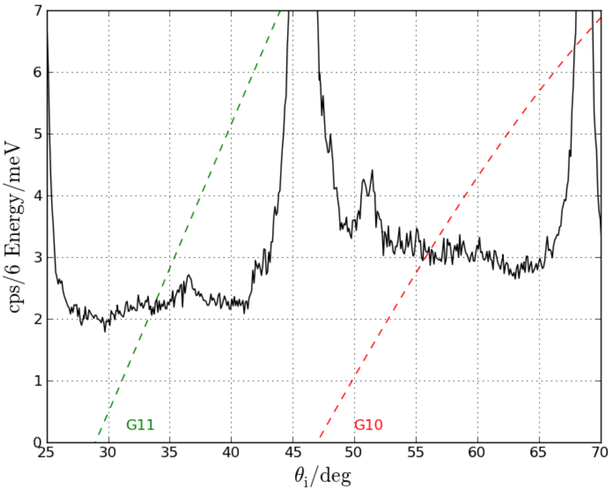

Figure 4.6.: Enlarged part of the <11> measurement in figure 4.1. The energy lines calculated using equation 4.1 lead to positive binding energies for the **G**-vectors $\mathbf{G_{10}}$ and $\mathbf{G_{11}}$.

considering interactions with every possible **G**-vector that would indicate a positive binding energy. As explained in section 2.6.3, the variation of the incident angle Θ_i changes only the parallel momentum $\mathbf{K_i}$, so for every **G**-vector there should be an easy expression for the possible bound state energies. Rewriting equation 2.45 leads to the desired expression.

$$|\epsilon_n(\Theta_i, \mathbf{k_i}, \mathbf{G})| = \frac{\hbar^2}{2m}\left[(|\mathbf{k_i}| \cdot \sin(\Theta_i) + |\mathbf{G}| \cdot \cos(\phi))^2 + (|\mathbf{G}| \cdot \sin(\phi))^2 - \mathbf{k_i}^2\right] \quad (4.1)$$

with ϕ, the angle between the scan direction and the **G**-vector. Using equation 4.1, all curves for fixed **G**-vectors that lead to positive binding energies can be plotted into the elastic spectrum, as displayed in figure 4.6.

Fortunately, only two **G**-vectors, namely $\mathbf{G_{10}}$ and $\mathbf{G_{11}}$ correspond to positive binding energies in the measured angular range and their angular range does not overlap in the typical energy range for interaction potentials. Since only three features are large enough to be clearly considered, the straightforward approach is to fit the clear features with a gaussian profile (1 in figure 4.7). The angle of the gaussian maximum is mapped back to the corresponding energy for a resonance with an available **G**-vector (2 in figure 4.7). Then the angular positions for resonances with other **G**-vectors for this energy are determined (3 in figure 4.7). Finally, possible resonance features at these positions are fitted with a gaussian (4 in figure 4.7). Figure 4.7 displays the result for one of the features. The other, very similar measurements of two further binding energies can be found in the appendix.

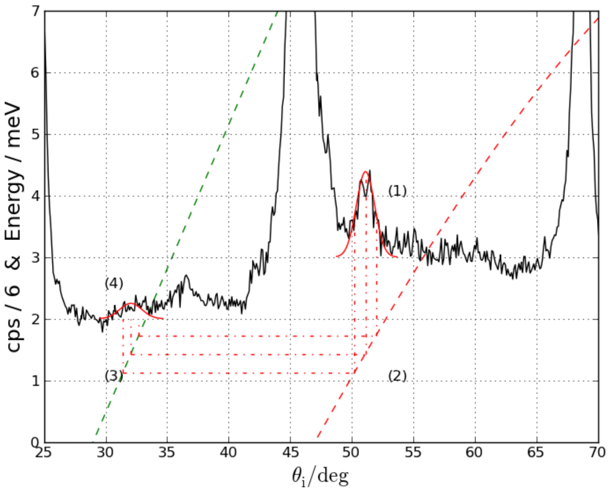

Figure 4.7.: Mapping of different features in the elastic spectrum to certain binding energies using equation 4.1. (1) The obvious peak is fitted with a gaussian. (2) The peak angle is mapped to the corresponding resonance energy with the available **G**-vector. (3) The angle of another **G**-vector interaction corresponding to the same energy is elicited. (4) Possible resonance features at this angle are fitted with a gaussian.

Figure 4.8 displays the identified resonance features in the considered elastic spectrum. A short explaination of the nomenclature: $(1,1)_2$ corresponds to a resonance of the incoming helium atoms with the $\mathbf{G_{11}}$-vector and the bound state with $n = 2$. The quantum number of the bound state is calculated in section 4.3.1, but already written here. The measured bound state energies were checked by calculating the angular position of expected resonances in the <10> scan in figure 4.1 (a). As figure 4.8 clearly shows, the expected positions yield a higher fluctuation in the background signal than the surroundings.

Since the signal to noise ratio of these measurements is very low, the measured energies were checked with every elastic measurement performed. The corresponding plots can be found in the Appendix.

The measured binding energies are:

$$\begin{aligned} E_0 &= (6.18 \pm 0.55)\ \mathrm{meV} \\ E_1 &= (3.49 \pm 0.28)\ \mathrm{meV} \\ E_2 &= (1.42 \pm 0.30)\ \mathrm{meV} \end{aligned} \tag{4.2}$$

The high uncertainty of E_0 can be explained with the dispersion of the bound energy

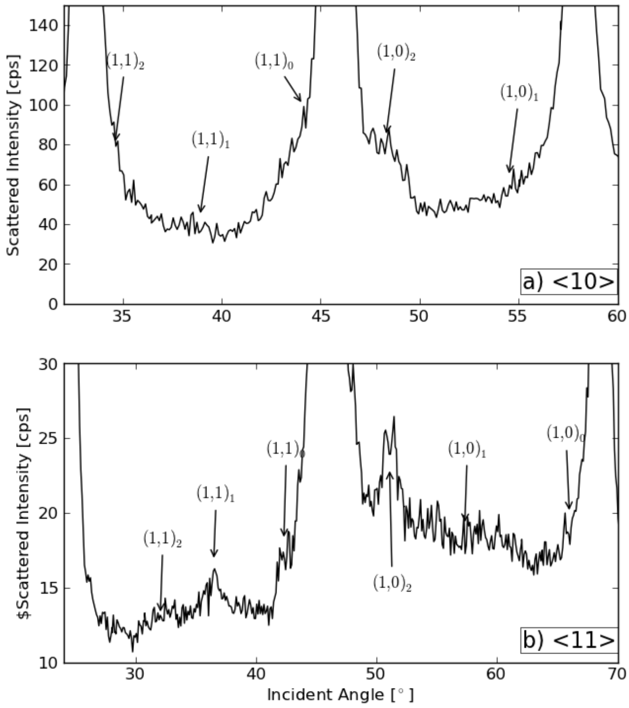

Figure 4.8.: Map of the measured resonance peaks in the <11> direction (b) and the calculated position of expected resonances in the <10> direction (a)

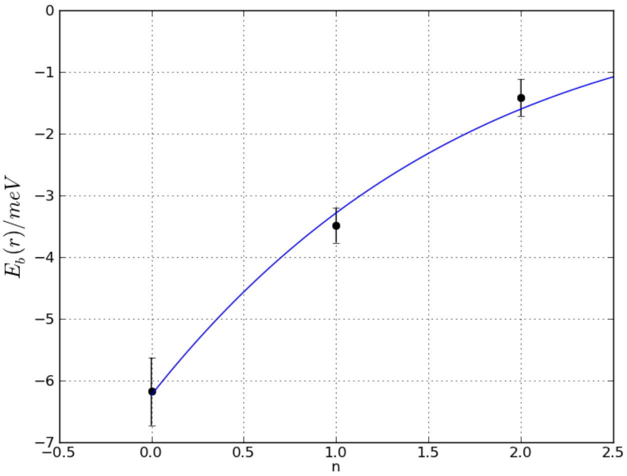

Figure 4.9.: Solution of a least-squares fit of equation 2.27 for the measured energy values 4.2. The integer parameter n is treated like a continuous variable to show the dependence of E_b.

levels and the averaging due to the angular uncertainty (see section 2.6.3).

4.3.1. He-Bi Interaction Potential

With the bound state energies 4.2 available, an estimate of the interaction potential parameters can be calculated. Figure 4.9 displays the solution of a least-squares fit of equation 2.27 for the measured bound state energies given in 4.2. The resulting parameters of the 3-9 potential given in equation 2.26 are

$$\begin{aligned} D &= (8.300 \pm 0.002)\ \text{meV} \\ \sigma &= (0.2891 \pm 0.0002)\ \text{nm} \end{aligned} \tag{4.3}$$

Figure 4.10 shows the calculated potential and its bound energy states. The calculated parameter for the potential depth D agrees well with values from previous measurements. The potential depth for Cu(117) and Ag(110) interaction with helium are 7.41 meV[40] and 5.7 meV[41] respectively.

4.3.2. Control Measurements in the Specular Intensity

Although the measured energy values correspond to the expected 3-9-potential shape very well, the measured features in the angular distribution are unsufficiently weak. To

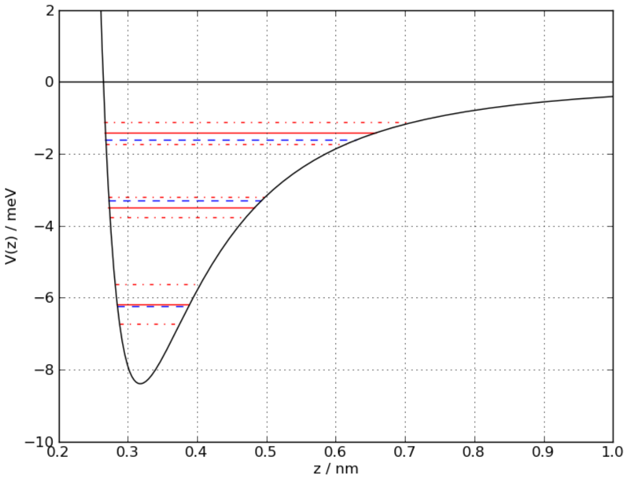

Figure 4.10.: Calculated perpendicular atom-surface interaction potential between helium and Bi(111). The red lines indicate the measured bound state energies and their uncertainties, the blue lines the analytical bound state values for this potential.

approve the energy values 4.2, the outcome of a different measurement was predicted. As explained in section 2.6.3, the surface resonance effects can be observed in three different measurements. The most popular one, the variation of the azimuthal angle γ is inexecutable on our apparatus, so the only remaining option is the temperature dependence of the specular peak.

The used formula for determinating the positions is the same as 4.1. The main difference is that the angle is now fixed at the specular peak position, and the magnitude of k_i is varied. This equation is plotted in figure 4.11. The intersection points in figure 4.11 determine the expected resonance temperatures given in table 4.3.

To validate the expected values, a specular intensity measurement was performed between 60 and 200 K. The specular intensity graph is plotted in figure 4.12. The overall temperature dependence of the helium intensity from the nozzle without the resonance effects would be $\sim \frac{1}{\sqrt{T}}$.[27] However, besides the continuous decrease of the overall intensity, some clear and intense features are recognizeable. The most prominent features in this measurement occur at 70.0 K, 86.8 K and the very broad feature at 108 K. The latter two seem to correspond to the $(1,-1)_2$ and the $(1,1)_0$ resonances. The high broadness of the $(1,1)_0$ feature can be explained by the variation of the potential depth by lateral position in the surface unit cell. Since the $n = 0$ bound state varies strongly in energy, the helium beam is resonant in a broad range of temperatures. The constant shift of approximately 8 K between the expected and the measured temperature values

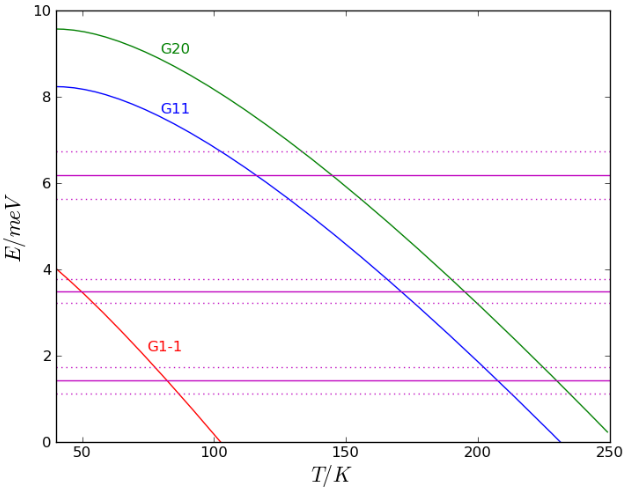

Figure 4.11.: Calculated energy lines for a resonant interaction of the specular peak in <11> direction with certain **G**-vectors. The expected resonance positions are the intersection points between the **G**-lines and the measured energy values.

Table 4.3.: Expected temperatures for resonant scattering effects on the specular peak as plotted in figure 4.11

RL … Resonance label
T … Temperature of the expected resonance

RL	T / K
$(1,-1)_1$	49.5
$(1,-1)_2$	82.1
$(1,1)_0$	116.2
$(2,0)_0$	144.9
$(1,1)_1$	170.5
$(2,0)_1$	194.7
$(1,1)_2$	207.6
$(2,0)_2$	229.8

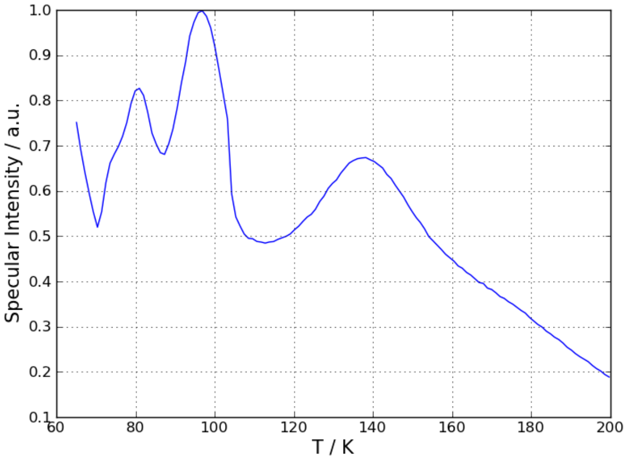

Figure 4.12.: Variation of the specular intensity with the nozzle temperature. The dip at 86 K and the broad feature at 115 K can be explained with the aid of the bound state resonance energies 4.2

originated from an intermediate temperature calibration of the apparatus.
The dominant dip at 70.0 K can not be explained using the most probable **G**-vectors. However, there could be an explanation for this dip in interactions with high-order **G**-vectors pointing in the opposite direction. Another option is that our understanding of the temperature dependence of the specular peak is incomplete. If additional effects are taken into account, the apparent shift of the resonance features in the specular measurements could be explained. This will be subject for further investigations.

5. Summary and Discussion

In the course of this work a complete picture of the He-Bi(111) interaction potential was derived from elastic helium atom scattering spectra. The corrugation function was calculated using an iterative procedure to fit the measured peak heights and was compared with previously calculated corrugation functions. Additionally, the vertical interaction potential was determined from elastic bound state resonances and checked by a measurement of the specular peak intensity as a function of the incident beam energy.
The performed measurements, i.e. the elastic angular spectrum and the temperature dependence of the specular peak are not the ideal methods to determine the bound state energies of the interaction potential, since in these measurements the resonant features are broadened by additional effects[37].
The resonance features in the elastic spectra mostly exhibit a very low intensity. The determination of the corresponding energy values is therefore very difficult and can give rise to additional errors. Also some of the more clear features could have appeared due to kinematical focussing effects, which were not considered in this thesis.
The determined energy values were used to fit the parameters of a 3-9 Potential as explained in section 2.6.1. These are the first measurements of the He-Bi(111) vertical interaction potential performed. The solutions are:

$$\begin{aligned} D &= (8.300 \pm 0.002) \text{ meV} \\ \sigma &= (0.2891 \pm 0.0002) \text{ nm} \end{aligned}$$

The iterative procedure to determine the surface corrugation also yields to some error possibilities. The sign of the used parameters for the heights of the specular peaks is undefined and assumed to be throughout positive. While this yields to a maximum value for the corrugation, the true shape can not be determined without a bootstrapping method. This might be subject for further investigations.
The calculated corrugation height relative to the surface lattice parameter is 16.3% which corresponds well to the 12% determined using common approximations.

The appearence of such a comperatively high surface corrugation on a material with a conducting surface is rather surprising. A possible origin of this fact could be the electronic hole pocket near the Γ-Point in the reciprocal space[14]. This local charge carrier distribution in k-space could account for a broad variation in real space. In future work the bismuth surface will be simulated ab initio to determine if the observed corrugation can be explained or if additional effects should be considered.

6. Bibliography

[1] D. Farías and K. Rieder, Reports on Progress in Physics **61**, 1575 (1998).

[2] J.P. Toennies, Journal of Physics: Condensed Matter **5**, A25 (1993).

[3] H. Hoinkes, Review of Modern Physics **52**, 933 (1980).

[4] D. E. Hulpke, *Helium Atom Scattering from Surfaces* (Springer Verlag Berlin Heidelberg New York, 1992).

[5] T. Engel and K.H. Rieder, in *Structural Studies of Surfaces* (Springer Berlin / Heidelberg, 1982).

[6] G. Benedek, G. Brusdeylins, C. Heimlich, J.P. Toennies, and U. Valbusa, Surface Science **178**, 545 (1986).

[7] G. Boato, P. Cantini, C. Salvo, R. Tatarek, and S. Terreni, Surface Science **114**, 485 (1982).

[8] P. Cantini and R. Tatarek, Surface Science **114**, 471 (1982).

[9] C. Ast and H. Höchst, Physical Review Letters **87**, 177602 (2001).

[10] M. Hengsberger, P. Segovia, M. Garnier, D. Purdie, and Y. Baer, The European Physical Journal B **17**, 603 (2000).

[11] B. Weitzel and H. Micklitz, Physical Review Letters **66**, 385 (1991).

[12] C. Vossloh, M. Holdenried, and H. Micklitz, Physical Review B **58**, 12422 (1998).

[13] M. Tian, N. Kumar, and M.H.W. Chan, Physical Reviev B **78**, 1 (2008).

[14] P. Hofmann, Progress in Surface Science **81**, 191 (2006).

[15] L. Díaz-Sánchez, A. Romero, and X. Gonze, Physical Review B **76**, 7 (2007).

[16] C. Kittel, *Introduction to Solid State Physics* (John Wiley & Sons, Inc., New York, Chichester, Brisbane, Toronto, Singapore, 1996), seventh edition ed.

[17] K. Oura, V. G. Lifshits, A. A. Saranin, A. V. Zotov, and M. Katayama, *Surface Science: An Introduction* (Springer, 2003).

[18] S. Hong and T. Raman, Physical Review B **71**, 245409 (2005).

[19] D. Farías, M. Patting, and K. Rieder, Journal of chemical physics **117**, 1797 (2002).

[20] R. Doak, *Atomic and Molecular Beam Methods Volume 2* (Oxford University Press, 1992), chap. 14 Single-Phonon Inelastic Helium Scattering, pp. 384–443.

[21] I. Estermann and O. Stern, Zeitschrift für Physik **61**, 95 (1930).

[22] G. Scoles, ed., *Atomic and Molecular Beam Methods Volume 2* (Oxford University Press, 1992).

[23] E. Zaremba and W. Kohn, Physical Review B **13**, 2270 (1976).

[24] E. Zaremba and W. Kohn, Physical Review B **15**, 1769 (1977).

[25] N. Lang, Physical Review Letters **46**, 842 (1981).

[26] J. Horne, S. Yerkes, and D. Miller, Surface Science **93**, 47 (1980).

[27] M. Mayrhofer-Reinhartshuber, Master's thesis, Technische Universität Graz, Institut für Experimentalphysik (2010).

[28] S. A. Safron, Advances In Chemical Physics, Vol 95 - Surface Properties **95**, 129 (1996).

[29] C. Nyeland and J.P. Toennies, Chemical Physics **321**, 285 (2006).

[30] M. Cole and T. Tsong, Surface Science **69**, 325 (1977).

[31] R. Smoluchowski, Phys. Rev. **60**, 661 (1941).

[32] N. Garcia, The Journal of Chemical Physics **67**, 897 (1977).

[33] U. Garibaldi, A. Levi, R. Spadacini, and G. Tommei, Surface Science **48**, 649 (1975).

[34] G. Benedek, G. Brusdeylins, R. B. Doak, J. G. Skofronick, and J.P.Toennies, Physical Reviev B **28**, 2104 (1983).

[35] A. Jardine, H. Hedgeland, G. Alexandrowicz, W. Allison, and J. Ellis, Progress in Surface Science **84**, 323 (2009).

[36] G. Benedek and J.P. Toennies, manuscript.

[37] V. Celli, N. Garcia, and J. Hutchison, Surface Science **87**, 112 (1979).

[38] M.Mayrhofer-Reinhartshuber, A. Tamtögl, P. Kraus, K.H. Rieder, and W.E. Ernst, vibrational dynamics and surface structure of Bi(111) from helium atom scattering measurements, unpublished.

[39] A. Tamtögl, M. Mayrhofer-Reinhartshuber, N. Balak, W.E. Ernst, and K.H. Rieder, Journal of Physics: Condensed Matter **22**, 1 (2010).

[40] J. Lapujoulade, Y. Lejay, and N. Papanicolaou, Surface Science **90**, 133 (1979).

[41] A. W. Dweydari and C. H. B. Mee, Physica Status Solidi **27**, 223 (1975).

A. Appendix

A.1. Iterative Method for Calculating the Surface Corrugation

Starting at

$$\sum_{\mathbf{G}} A_{\mathbf{G}} exp\{i\,[\mathbf{G}\cdot\mathbf{R} \;+\; k_{\mathbf{G}z}\xi(\mathbf{R})]\} \;=\; -exp\{ik_{iz}\xi(\mathbf{R})\} \tag{A.1}$$

To bypass the main problem, the appearence of $\xi(\mathbf{R})$ in both terms, one first extracts the $\mathbf{G} \;=\; 0$ part.

$$A_{\mathbf{0}} exp\{ik_{\mathbf{G_0}z}\xi(\mathbf{R})\} \;+\; \sum_{\mathbf{G'}} A_{\mathbf{G'}} exp\{i\,[\mathbf{G'}\cdot\mathbf{R} \;+\; k_{\mathbf{G'}z}\xi(\mathbf{R})]\} \;=\; -exp\{ik_{iz}\xi(\mathbf{R})\} \tag{A.2}$$

Whilst $k_{\mathbf{G_0}z} \;=\; k_{iz}$. This leads to

$$\sum_{\mathbf{G'}} A_{\mathbf{G'}} exp\{i\,[\mathbf{G'}\cdot\mathbf{R} \;+\; k_{\mathbf{G'}z}\xi(\mathbf{R})]\} \;=\; -\,(A_{\mathbf{0}} \;+\; 1)\, exp\{ik_{iz}\xi(\mathbf{R})\} \tag{A.3}$$

using the normalization of the intensities[1]

$$\sum_{\mathbf{G}} P_{\mathbf{G}} \;\overset{!}{=}\; 1 \tag{A.4}$$

and

$$P_{\mathbf{G}} \;=\; \frac{|k_{\mathbf{G}z}|}{|k_{iz}|} A_{\mathbf{G}} A^{*}_{\mathbf{G}} \tag{A.5}$$

following expression can be derived:

$$\sum_{\mathbf{G'}} \pm\sqrt{\frac{|k_{iz}|}{|k_{\mathbf{G}z}|} P_{\mathbf{G'}}}\, exp\{i\,[\mathbf{G'}\cdot\mathbf{R} \;+\; k_{\mathbf{G'}z}\xi(\mathbf{R})]\} \;=\; -\left(\pm\sqrt{P_{\mathbf{0}}} \;+\; 1\right) exp\{ik_{iz}\xi(\mathbf{R})\} \tag{A.6}$$

In order to solve this equation all the roots are assumed to be positive. Further simulations could determine the right signs by simulating the scattering peaks from the resultant corrugation functions. For a solution also only the real part is of interest.

$$\begin{aligned} \sum_{\mathbf{G'}} \sqrt{\frac{cos\theta_i}{cos(\theta_{SD} \;-\; \theta_i)}} \cdot \sqrt{P_{\mathbf{G'}}} \cdot cos\,[\mathbf{G'}\cdot\mathbf{R} \;+\; |\mathbf{k_i}| \cdot cos(\theta_{SD} \;-\; \theta_i)\xi(\mathbf{R})] \;&=\; \\ =\; -\left(\sqrt{P_{\mathbf{0}}} \;+\; 1\right) cos\,(|\mathbf{k_i}| cos\theta_i \xi(\mathbf{R}))& \end{aligned} \tag{A.7}$$

To get a starting point of the iteration, the assumption

$$\mathbf{G}' \cdot \mathbf{R} \;\gg\; |\mathbf{k_i}| \cdot cos(\theta_{SD} \;-\; \theta_i)\xi(\mathbf{R}) \tag{A.8}$$

is made. This is only valid for $\mathbf{R} \gg 0$ and small $\xi(\mathbf{R})$. In all cases where this approximation will not hold, the function will converge. At these points the starting corrugation is set to the average elevation of the rest of the function. The functions for the iteration are:

$$\xi^0(\mathbf{R}) \;=\; \frac{1}{|\mathbf{k_i}| \cdot cos(\theta_i)} \cdot arccos\left[-\frac{1}{\sqrt{P_\mathbf{0}} \;+\; 1}\sum_{\mathbf{G}'}\sqrt{P_{\mathbf{G}'}\frac{cos\theta_i}{cos(\theta_{SD}-\theta_i)}} \cdot cos(\mathbf{G}'\mathbf{R})\right] \tag{A.9}$$

for the starting value and

$$\begin{aligned}\xi^0(\mathbf{R}) \;=\; & \frac{1}{|\mathbf{k_i}| \cdot cos(\theta_i)} \cdot arccos\left[-\frac{1}{\sqrt{P_\mathbf{0}} \;+\; 1}\sum_{\mathbf{G}'}\sqrt{P_{\mathbf{G}'}\frac{cos\theta_i}{cos(\theta_{SD}-\theta_i)}} \cdots\right. \\ & \left.\cdots cos\left[\mathbf{G}'\mathbf{R} \;+\; |\mathbf{k_i}| \cdot cos(\theta_{SD}-\theta_i)\xi^n(\mathbf{R})\right]\right]\end{aligned} \tag{A.10}$$

A.2. Determination of the Bound State Energies for $n = 0$ and $n = 1$

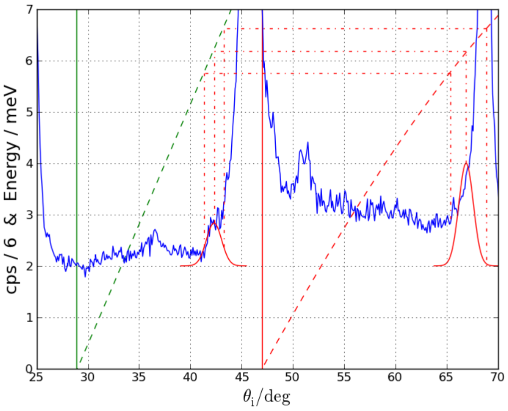

Figure A.1.: Mapping of different features in the elastic spectrum to certain binding energies using equation 4.1. Bound state energy with $n = 0$

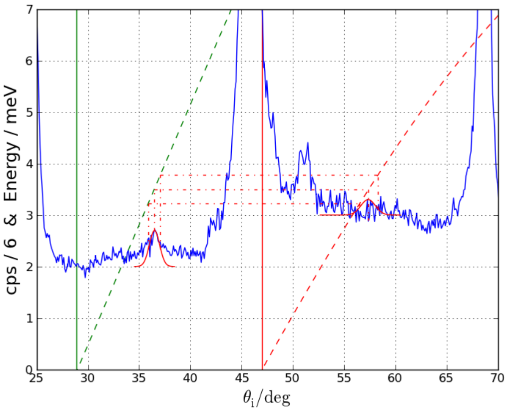

Figure A.2.: Mapping of different features in the elastic spectrum to certain binding energies using equation 4.1. Bound state energy with $n = 1$

A.3. Maps of Bound State Resonances in the Elastic Scattering Spectra

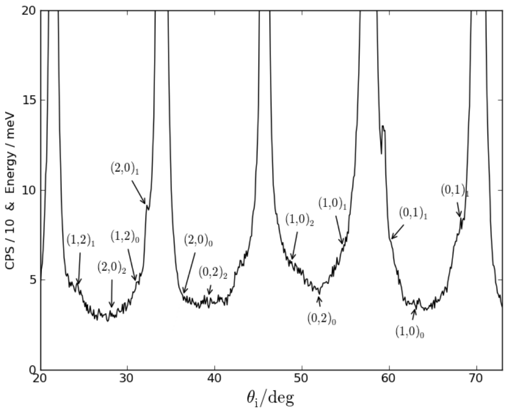

Figure A.3.: Map of the found resonance features in the <10> direction at a nozzle temperature of 75 K and a sample temperature of 118 K

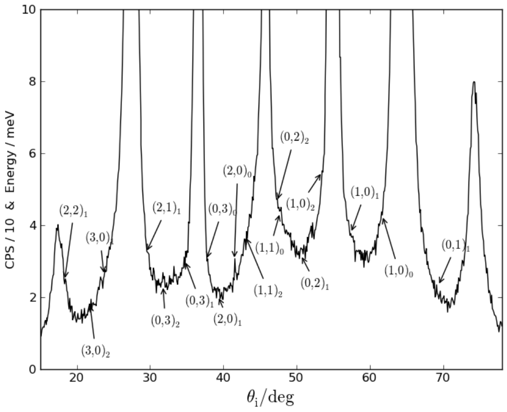

Figure A.4.: Map of the found resonance features in the <10> direction at a nozzle temperature of 130 K and a sample temperature of 118 K

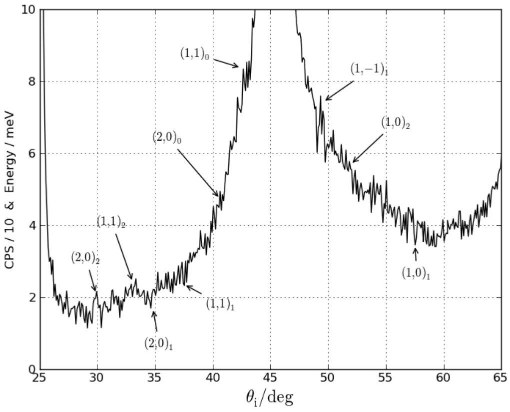

Figure A.5.: Map of the found resonance features in the <11> direction at a nozzle temperature of 75 K and a sample temperature of 300 K

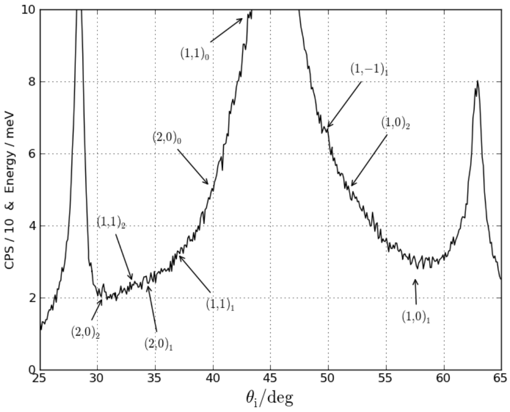

Figure A.6.: Map of the found resonance features in the <11> direction at a nozzle temperature of 75 K and a sample temperature of 113 K

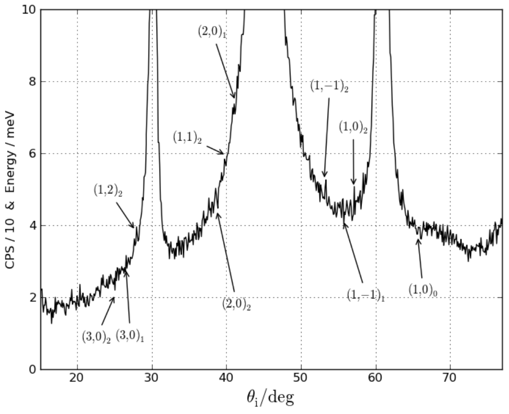

Figure A.7.: Map of the found resonance features in the <11> direction at a nozzle temperature of 135 K and a sample temperature of 113 K

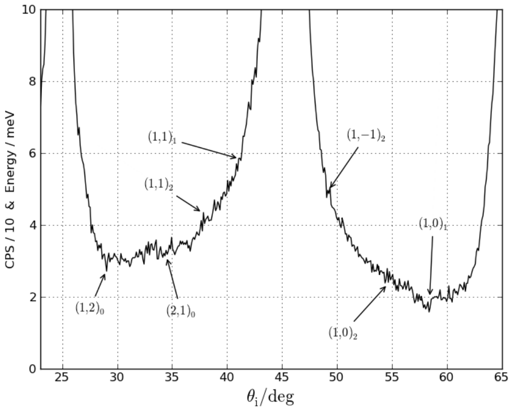

Figure A.8.: Map of the found resonance features in the <11> direction at a nozzle temperature of 105 K and a sample temperature of 300 K

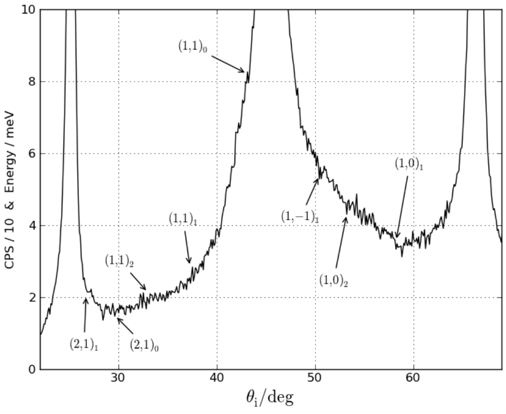

Figure A.9.: Map of the found resonance features in the <11> direction at a nozzle temperature of 85 K and a sample temperature of 300 K

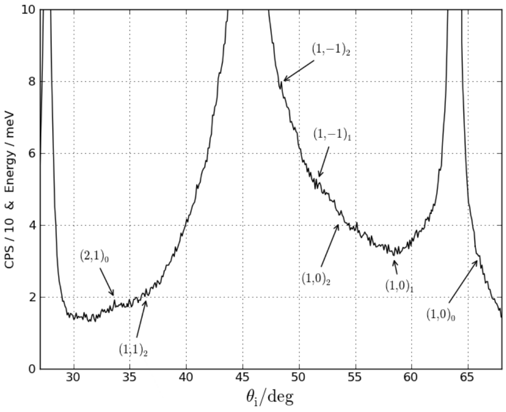

Figure A.10.: Map of the found resonance features in the <11> direction at a nozzle temperature of 95 K and a sample temperature of 300 K

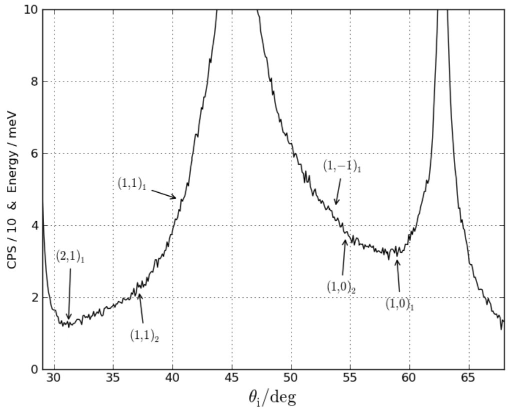

Figure A.11.: Map of the found resonance features in the <11> direction at a nozzle temperature of 105 K and a sample temperature of 300 K

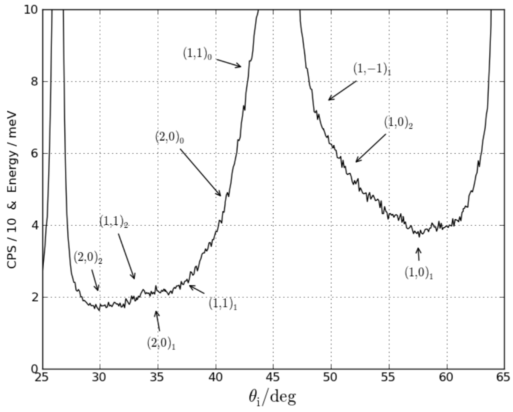

Figure A.12.: Map of the found resonance features in the <11> direction at a nozzle temperature of 75 K and a sample temperature of 300 K

Acknowledgements

First of all I have to thank Prof. Giorgio Benedek for his constant support and relentless motivation. Without his numerous tipps and hints most of this work would not have been possible. I also want to thank my supervisor Prof. Wolfgang E. Ernst for the overwhelming opportunity to go to Milano to learn as much as possible from the experts of the field of surface simulations and helium atom scattering.

I furthermore want to thank all my colleagues for their patient support and especially Toni Tamtögl for reading and correcting this work over and over again and Michael Mayrhofer for numerous discussions about the sometimes challenging theory.

Besides those two I want to thank Alexander Volk and Günter Krois who, like my direct colleagues helped to blow some steam off with a quick game of Go or some bouldering.

I also owe the ladies from the secretary a thank you for helping me through the buerocratic jungle of compensation of travel expenses.

Above them all I want to thank my family and my girlfriend for their never ending support whenever I needed it.